Die approbierte Originalversion dieser Diplom-/Masterarbeit ist an der Hauptbibliothek der Technischen Universität Wien aufgestellt (http://www.ub.tuwien.ac.at).

The approved original version of this diploma or master thesis is available at the main library of the Vienna University of Technology (http://www.ub.tuwien.ac.at/englweb/).

MASTER THESIS

Dielectrophoresis-based Characterization and Separation of Cells

Submitted at the Faculty of Electrical Engineering, Vienna University of Technology
in partial fulfillment of the requirements for the degree of
Master of Sciences (Diplomingenieur)

under supervision of

Univ.Prof. Dr. Michiel J. Vellekoop
Dipl.-Ing. Sander van den Driesche

by

Dietmar Puchberger-Enengl
Matr.Nr. 0226258
St.Johann 130, 3352 St.Peter/Au

November, 2009

Abstract

Dielectrophoresis, the motion of polarizable particles in a non-uniform electric field, is a promising technique for on-chip handling of biological particles like cells and bacteria. Multiple microelectrode devices were designed, simulated and fabricated to investigate different aspects of cell separation by dielectophoresis (DEP). Besides the dielectrophoretic force, the electric field induces AC electroosmosis and electrothermal effects. To minimize these undesired effects, adequate operating conditions were defined.
Dielectrophoretic and electrorotational spectra were determined for T-lymphocytes, *Saccharomyces cerevisiae*, *Lactobacillus casei*, *Nannochloropsis sp.* and *Isochrysis galbana*. Dielectric properties of these cell types were estimated by applying a multiple shell model. The obtained data was used to find optimal separation conditions for cell mixtures.
The advantages and disadvantages of different dielectrophotretic separation methods: positive and negative DEP forces, negative DEP force and travelling wave DEP are evaluated and compared.

Kurzfassung

Dielektrophorese, die Bewegung polarisierbarer Teilchen in einem inhomogenen elektrischen Feld, ist eine vielversprechende Technik zur on-Chip Manipulation von biologischen Teilchen wie Zellen und Bakterien. Um die Separation von Zellen mittels Dielektrophorese (DEP) zu untersuchen, wurden verschiedene Mikroelektroden-Chips entworfen, simuliert und hergestellt. Durch das elektrische Feld treten neben Dielektrophorese auch AC Elektroosmose und elektrothermische Effekte auf. Um diese unerwünschten Effekte zu minimieren, wurden entsprechende Betriebsbedingungen definiert.
Dielektrophorese- und Elektrorotationsspektren wurden für T-Lymphocyten, *Saccharomyces cerevisiae*, *Lactobacillus casei*, *Nannochloropsis sp.* und *Isochrysis galbana* gemessen. Die dielektrischen Eigenschaften dieser Zellen wurden mit Hilfe eines vereinfachten Modells mit konzentrischen Hüllen berechnet. Diese Daten wurden benutzt, um optimale Bedingungen für die Separation verschiedener Zelltypen zu bestimmen.
Die Vor- und Nachteile der Separationsmethoden: Separation mit positiver und negativer Dielektrophorese, Separation mittels negativer Dielektrophorese und Separation durch Wanderwellen-Dielektrophorese werden diskutiert und verglichen.

Acknowledgements

This project is a part of the EU Marie Curie Research Training Network (MRTN) "On-Chip Cell Handling and Analysis" CellCheck. Project no. MRTN-CT-2006-035854.

First and foremost, I would like to thank Univ. Prof. Dr. Michiel J. Vellekoop for the opportunity to work in such an interesting field of research, his advices and motivating words. Special thanks to my adviser Dipl.-Ing. Sander van den Driesche for his support, encouragement and time for constructive conversations.
I would like to thank the colleagues at the Institute of Sensor and Actuator Systems Dr. Stefan Kostner for his advices, Ing. Edeltraud Svasek and Ing. Peter Svasek for the realization of the devices and Univ. Lektor Günther Stangl for borrowing me equipment.
I would like to express my deep gratitude to my parents Franz Puchberger-Enengl and Hildegard Puchberger-Enengl for their financial support all the years. Special thanks to Michaela Zeitlhofer for her understanding and mental support.

Table of Contents

Nomenclature

$cDEP$	conventional dielectrophoresis
$gDEP$	generalized dielectrophoresis
$nDEP$	negative dielectrophoresis
$pDEP$	positive dielectrophoresis
$twDEP$	traveling wave dielectrophoresis
ROT	electrorotation
$ACEO$	AC electro osmosis
ETE	electrothermal effects
c_m	membrane capacitance
d	distance
E	electric field strength
$\mathbf{F}$	force vector
f_{C0}	crossover frequency
g	gravitational acceleration
g_m	membrane transconductance
h_c	channel height
$\underline{K}$	Clausius-Mosotti factor
k	wave number
k_R	ROT scaling factor
k_T	thermal conductivity
$\mathbf{p}$	dipole moment
Re	Reynolds number
R	particle radius
$\mathbf{T}$	torque vector
T	temperature
V	particle volume
v_m	medium velocity
v_p	particle velocity

$\mathbf{x}, \mathbf{y}, \mathbf{z}$	orthogonal unit vectors
δ	shell thickness
ϵ	dielectric permittivity
Φ	phase angle
φ	electric potential
κ	reciprocal of the Debye length
λ	wavelength
η	viscosity
ρ_m	medium density
ρ_p	particle density
σ	electric conductivity
ω	angular frequency

1 Introduction

Laboratories on a chip are promising devices for clinical diagnostics and environmental monitoring. Miniaturized, inexpensive and automated devices can be used at point of care and in environments lacking infrastructure or skilled technicians. The manipulation of biological particles like cells, bacteria, viruses, DNA and RNA is an important task in such devices. Analyses in Lab-on-chip devices are performed on single cells or cell cultures, much smaller than in conventional macro devices. An advantage of the reduced reaction volumes is that smaller amounts of samples and chemicals are required, which reduces the costs.
Dielectrophoresis, the motion of small particles (10^{-7} m - 10^{-3} m) in a non-uniform electric field, has been investigated the last few decades to manipulate biological particles. Dielectrophoresis (DEP) can be used as a non-invasive technique for selective manipulation of bio-particles. The force exerted on the particles depends on their dielectric properties and size. Therefore, a separation of cells without the need of antibodies or other labelling techniques is possible.
Numerous dielectrophoretic applications have been investigated in biotechnology, e.g. purification of cell cultures, detection and isolation of pathogens, separation of cancerous and normal cells or studies of morphological changes. Considerable research has been published on positioning [MRV07] and separation of different cells [GWHB97], bacteria [CCHC07] and viruses [MHG99] and the estimation of dielectric cell properties [YHW+99, WWK07].
In this work, multiple microelectrode devices were designed, simulated and fabricated to separate human cells, bacteria, yeast and algae cells by means of dielectrophoresis. Besides the dielectrophoretic force, undesired side effects related to the electric field occur, contributing to the overall particle motion. The theory of AC electrokinetic effects is illustrated in Chapter 2. To investigate the influence of these effects, basic DEP experiments under varying conditions were performed.
In order to achieve well defined cell movement it is important to know cells' responses to an electric field. Since biological cells are inhomogeneous, complex particles, a simplified model is desired. With a multi-shell model the dielectric parameters of cell compartments can be derived from experimental data. The obtained parameters can be used to predict the DEP response at varying medium properties and frequencies.
For continuous separation experiments cell mixtures are pumped through the microfluidic devices containing different electrode structures. The DEP force is directed perpendicularly to the flow, selectively deflecting different cells. Finite element simulations have been used to analyze the separation process. Measurements utilizing different separation methods were performed and are compared.

2 Theory

Biological cells in an aqueous medium exposed to an inhomogeneous AC electric field exhibit motion under different physical effects. These effects and the resulting forces are discussed in the following subsections.
To estimate the Clausius-Mosotti factor, which determines the dielectrophoretic forces, an appropriate model of cells is needed. Therefore, multi-shell models are illustrated in Section 2.2. Simulation results for different cell types and models are shown in Section 2.3.

2.1 Physical Effects

If a particle is suspended in a medium of different permittivity and conductivity and exposed to an electric field, free charge is accumulated at the interface between the particle and the medium. The so formed dipole is aligned with the field when the particle polarizability is higher than that of the medium and vice versa. Considering a particle subjected to a non-uniform electric field, leads to an imbalance of forces on the induced dipole and thus to particle motion (Fig. 2.1). A particle with $\epsilon_p > \epsilon_m$ moves towards the high electric field region under positive dielectrophoresis (pDEP). The opposite is true for $\epsilon_p < \epsilon_m$, which is termed as negative dielectrophoresis (nDEP). If the electric field is not non-uniform but rotating, a circular movement of the particle can be observed, called electrorotation (ROT).

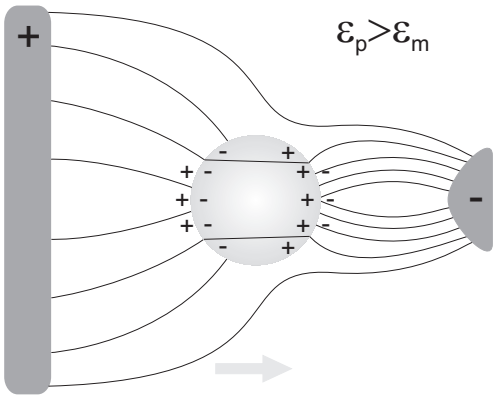

Figure 2.1: Positive dielectrophoresis: A polarizable particle ($\epsilon_p > \epsilon_m$) in a non-uniform electric field. The force is directed towards the high electric field region.

DEP and ROT effects can be described by using the effective moment method or the Maxwell stress tensor formulation. This section provides an overview of the the effective moment method because of its ease of use and favorable agreement with experiments. For a detailed description refer to Jones [Jon95, Jon03]. However, the most rigorous approach to derive DEP forces and ROT torques is the Maxwell stress tensor formulation [SS85, WWG97].
Beside these effects AC electro osmosis, Joule heating and gravity contribute to the behaviour of cells in microfluidic devices. Because the diameter of cells is above $1\,\mu m$, Brownian motion can be neglected and is left out in this work.

2.1.1 Dielectrophoresis

As defined by Pohl, dielectrophoresis is the motion of polarizable particles exposed to a non-uniform electric field [Poh51, PC71]. If the electric field is only slightly non-uniform the DEP force on spherical particles can be approximated by

$$\mathbf{F}_{DEP} = 2\pi\epsilon_m R^3 \mathcal{R}[\underline{K}(\omega)]\nabla E_{rms}^2 \tag{2.1}$$

where R is the particle radius, ϵ_m is the permittivity of the medium, E_{rms} is the electric field strength and $\mathcal{R}[\underline{K}(\omega)]$ refers to the real part of the Clausius-Mosotti factor (2.2).

$$\underline{K}(\omega) = \frac{\underline{\epsilon}_p - \underline{\epsilon}_m}{\underline{\epsilon}_p + 2\underline{\epsilon}_m} \tag{2.2}$$

$\underline{\epsilon}_m$ and $\underline{\epsilon}_p$ are the complex permittivities ($\underline{\epsilon_i} = \epsilon_i + \sigma_i/j\omega$) of the medium and the particle, respectively.

In the following derivation of Eq. 2.1 we assume a dipole exposed to an externally applied electric field. If the field is nonuniform the two charges will experience a net force due to local differences of the vector field $\mathbf{E}$ (Fig. 2.2). The sum of the forces gives

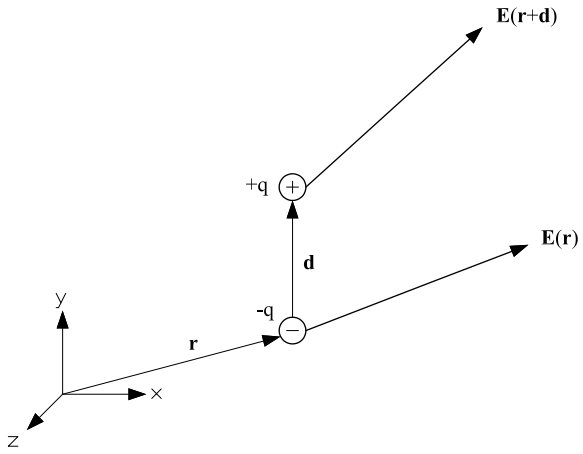

Figure 2.2: Net force on a small dipole of strength $\mathbf{p} = q\mathbf{d}$ in a non-uniform electric field. [Jon95, p. 7]

$$\mathbf{F} = q\mathbf{E}(\mathbf{r} + \mathbf{d}) - q\mathbf{E}(\mathbf{r}). \tag{2.3}$$

In the case that the distance $\mathbf{d}$ between the two charges is small compared to the characteristic dimension of the electric field non-uniformity, the electric field can be expressed using a vector Taylor series expansion (2.4) around $\mathbf{r}$.

$$f(\mathbf{r} + \mathbf{d}) = \sum_{i=0}^{\infty} \frac{1}{i!}(\mathbf{d} \cdot \nabla_{\acute{\mathbf{r}}})^i f(\acute{\mathbf{r}})|\acute{\mathbf{r}} = \mathbf{r} \tag{2.4}$$

When only the zeroth- and first-order terms are taken into account, the following result for the force on an infinitesimal dipole is obtained.

$$\mathbf{F}_{dipole} = \mathbf{p} \cdot \nabla \mathbf{E} \tag{2.5}$$

The basis of the effective moment method is the hypothesis that the effective dipole $\mathbf{p}$ produces the same dipolar field as the original particle when placed in same dielectric medium. The electrostatic potential of a point dipole is given by Eq. 2.6.

$$\varphi = \frac{p\ cos\theta}{4\pi\epsilon_m r^2} \tag{2.6}$$

Assume a dielectric sphere of radius R which is suspended in a fluid of permittivity ϵ_m and subjected to an electric field of magnitude E_0. If there are no free charges in the space the electrostatic potential satisfies Laplace's equation. The solution for the potential takes the form:

$$\varphi_1(r,\theta) = -E_0 r\ cos\theta + \frac{\epsilon_p - \epsilon_m}{\epsilon_p + 2\epsilon_m}\frac{E_0 R^3\ cos\theta}{r^2}, \qquad r > R \tag{2.7a}$$

$$\varphi_2(r,\theta) = -E_0 \frac{3\epsilon_m}{\epsilon_p + 2\epsilon_m} cos\theta r, \qquad r < R. \tag{2.7b}$$

Comparing Eq. 2.6 to the induced dipole term in Eq. 2.7a yields the expression for the effective dipole moment, which is:

$$p = 4\pi\epsilon_m R^3 K E_0. \tag{2.8}$$

Keeping these results in mind, the time-averaged dielectrophoretic force on a lossy particle (ϵ_p, σ_p) in a slightly nonuniform, sinusoidally time-varying electric field is

$$\begin{aligned} < \mathbf{F}_{DEP} > = & \frac{1}{2}\,\mathcal{R}[\underline{\mathbf{p}} \cdot \nabla \underline{\mathbf{E}}^*] \\ = & \frac{1}{2}\,\mathcal{R}[4\pi\epsilon_m R^3 \underline{K\mathbf{E}} \cdot \nabla \underline{\mathbf{E}}^*] \\ = & \ 2\,\pi\epsilon_m R^3 \mathcal{R}[\underline{K}\frac{1}{2}\nabla E^2] \\ = & \ 2\,\pi\epsilon_m R^3 \mathcal{R}[\underline{K}]\nabla E^2_{rms} \end{aligned} \tag{2.9}$$

where the last line exactly takes the form of Equation 2.1. If the non-uniformity of the electric field is significant, higher order linear multipoles are needed for force calculation. However, the dipole approximation is quite robust and suitable for most electrode structures. An exclusion is the planar quadrupolar electrode geometry where the dipole force in the center is zero and the particle is levitated by the quadrupolar force [Jon03].

2.1.2 Electrorotation

As previously, the starting point for the derivation of electrorotation (ROT) is an infinitesimal dipole. The torque exerted by an electric field on an infinitesimal dipole is given by [Jon95, p. 8]:

$$\mathbf{T}_{dipole} = \mathbf{p} \times \mathbf{E}. \tag{2.10}$$

Assume a counter-clockwise rotating electric field which takes the vector phasor form

$$\underline{\mathbf{E}}(x, y) = E_0(\mathbf{x} - j\mathbf{y}) \tag{2.11}$$

where $\mathbf{x}$ and $\mathbf{y}$ are orthogonal unit vectors. Using the results of section 2.1.1 the time-averaged torque on a lossy particle (ϵ_p, σ_p) in a rotating field results in

$$\begin{aligned} < \mathbf{T}_{dipole} > = & \frac{1}{2}\,\mathcal{R}[\underline{\mathbf{p}} \times \underline{\mathbf{E}}^*] \\ = & \frac{1}{2}\,\mathcal{R}[4\pi\epsilon_m R^3 \underline{K\mathbf{E}} \times \underline{\mathbf{E}}^*] \\ = & \ 2\,\pi\epsilon_m R^3 \mathcal{R}[\underline{K} E_0(\mathbf{x} - j\mathbf{y}) \times E_0(\mathbf{x} + j\mathbf{y})] \\ = & \ -4\,\pi\epsilon_m R^3 \mathcal{I}[\underline{K}] E_0^2 \mathbf{z}. \end{aligned} \tag{2.12}$$

When the particle is in a viscous solution a drag torque (Eq. 2.13) acts on it in opposite direction.

$$\mathbf{T}_{drag} = \quad 8\pi\eta\Omega R^3 \tag{2.13}$$

A uniform rotation Ω is achieved when both torques are equal:

$$\Omega = \quad -\frac{\epsilon_m \mathcal{I}[\underline{K}] E_0^2}{2\eta} \tag{2.14}$$

where η is the viscosity of the fluid [WWK07].

2.1.3 Travelling Wave Dielectrophoresis

Linear motion of particles and cells induced by travelling electric fields was first described by Masuda *et al.* in the low frequency range of 0.1Hz - 100Hz [MWI87, MWK88]. The travelling field was produced by applying multi-phase voltage to a series of parallel microelectrodes.

Later work shows an asynchronous motion of cells in the kHz frequency range where nDEP occurs. In this case, cells are levitated above the linear arranged electrodes and move perpendicularly to them. If pDEP is present, cells are attracted towards the electrodes and might get trapped, which makes travelling wave dielectrophoresis (twDEP) less effective [FHM91].

The time-averaged twDEP force acting on a particle can be written as:

$$< \mathbf{F}_{twDEP} >= \quad -\frac{4\pi^2 \epsilon_m R^3 \mathcal{I}[\underline{K}] E_0^2}{\lambda} \tag{2.15}$$

where λ is the wavelength of the travelling electric field that is equal to the distance between electrodes of the same phase [HWTP93].

Wang *et al.* derived a theory that unifies the expressions of cDEP (Eq. 2.1) and twDEP (Eq.2.15) forces [WHBG94, WHH+94]. Their main results are summarized in the following.

Consider a sinusoidal electric field of angular frequency ω in a general form, which is

$$\begin{aligned} \mathbf{E} = & \quad E_x(t)\mathbf{x} + E_y(t)\mathbf{y} + E_z(t)\mathbf{z} \\ = & \quad \sum_{a=x,y,z} E_{\alpha 0}(x,y,z)\ cos(\omega t + \Phi_\alpha(x,y,z))\mathbf{a}. \end{aligned} \tag{2.16}$$

Note that the magnitude and phase of each field component are assumed to be spatial functions. The induced dipole moment for a lossy particle exposed to the above electric field is obtained as

$$\mathbf{p} = p_x(t)\mathbf{x} + p_y(t)\mathbf{y} + p_z(t)\mathbf{z} \tag{2.17}$$

where

$$\begin{aligned} p_x(t) = & \quad 4\pi\epsilon_m R^3 E_{x0} |\underline{K}| cos(\omega t + \Phi_x - \Phi_m) \\ = & \quad 4\pi\epsilon_m R^3 E_{x0} (\mathcal{R}[\underline{K}] cos(\omega t + \Phi_x) - \mathcal{I}[\underline{K}] sin(\omega t + \Phi_x)). \end{aligned} \tag{2.18}$$

Φ_m is the phase angle by which the dipole moment lags behind the electric field [WHBG94]. Electric fields of practical interest have frequencies below 1GHz and, therefore, the wavelength is much larger than the characteristic length of typical electrode geometries. As a consequence, $\partial E_x(t)/\partial y$ is equal to $\partial E_y(t)/\partial x$ and Eq. 2.5 can be rewritten as [WHH+94]

$$\mathbf{F}_{dipole} = \sum_{a=x,y,z} p_x(t)\frac{\partial E_x(t)}{\partial a} + p_y(t)\frac{\partial E_y(t)}{\partial a} + p_z(t)\frac{\partial E_z(t)}{\partial a}. \tag{2.19}$$

Using Eqs. 2.16 and 2.18 the first term of Eq. 2.19 is

$$\begin{aligned} p_x(t)\frac{\partial E_x(t)}{\partial a} = 4\pi\epsilon_m R^3 E_{x0}(\mathcal{R}[\underline{K}]cos(\omega t+\Phi_x) - \mathcal{I}[\underline{K}]sin(\omega t+\Phi_x)) \\ \times(\frac{\partial E_{x0}}{\partial a}cos(\omega t+\Phi_x) - \frac{\partial \Phi_x}{\partial a}E_{x0}sin(\omega t+\Phi_x)). \end{aligned} \tag{2.20}$$

Averaging this expression over a time much larger than the field period gives:

$$< p_x(t)\frac{\partial E_x(t)}{\partial a} >= 2\pi\epsilon_m R^3(\mathcal{R}[\underline{K}]E_{x0}\frac{\partial E_{x0}}{\partial a} + \mathcal{I}[\underline{K}]E_{x0}^2\frac{\partial \Phi_x}{\partial a}). \tag{2.21}$$

As the second and third terms of Eq. 2.19 have similar forms, the complete expression for the gDEP force is given by

$$< \mathbf{F}_{gDEP} >= 2\pi\epsilon_m R^3(\mathcal{R}[\underline{K}]\nabla E_{rms}^2 + \mathcal{I}[\underline{K}](E_{x0}^2\nabla\Phi_x + E_{y0}^2\nabla\Phi_y + E_{z0}^2\nabla\Phi_z)). \tag{2.22}$$

By using the substitutions, $\Phi_x = kx = 2\pi x/\lambda$, and $\Phi_y = \Phi_z = const.$ the second term can be identified as the twDEP force of Eq. 2.15.

2.1.4 Stokes Drag

The governing equation for fluid motion in microfluidic devices is the incompressible Navier-Stokes equation. For small particles with a Reynolds number $Re = 2\rho R v_m/\eta << 1$ the Navier-Stokes equation reduces to the linear Stokes equation. This yields the Stokes drag for the steady state motion of a spherical particle in an incompressible fluid [Bru08].

$$\mathbf{F}_{drag} = 6\pi\eta R(v_m - v_p) \tag{2.23}$$

where v_m and v_p are the velocities of the medium and the particle, respectively.

2.1.5 Particle Sedimentation

For a particle of density ρ_p suspended in a medium of density ρ_m the gravitational force is given by

$$\mathbf{F}_g = gV(\rho_p - \rho_m) \tag{2.24}$$

where V is the particle volume and g is the gravitational acceleration. If the cell density is higher than that of the medium the gravitational force causes sedimentation. Assuming steady state motion of the particle, where an equilibrium of Eq. 2.24 and the drag force (Section 2.1.4) is reached, leads to a sedimentation velocity of

$$v_p = \frac{gV(\rho_p - \rho_m)}{6\pi\eta R}. \tag{2.25}$$

Typical values for human cells ($\rho_p = 1050\,\mathrm{kg/m^3}$, $R = 6\,\mu\mathrm{m}$) and values for water at 20°C ($\eta = 1.003\,\mathrm{mPa\,s}, \rho_m = 998\,\mathrm{kg/m^3}$) yield a sedimentation velocity of $v_p = 4.07\,\mu\mathrm{m/s}$.

2.1.6 AC Electroosmosis

The effect of AC electro-osmosis (ACEO) is fluid motion due to the interaction of an electrolyte with a charged surface. Ions of opposite charge to the electrodes are attracted to the surface and form an electrical double layer (Debye layer). If the electric field at the surface has a tangential component, the ions begin to move and pull the bulk liquid along by viscous drag.

The ACEO velocity is given by

$$< v_{ACEO} > = \frac{\epsilon_m \varphi_0^2 \Psi^2}{8\eta d(1+\Psi^2)^2} \tag{2.26a}$$

$$\Psi = \frac{\epsilon_m}{2\sigma_m}\pi\kappa d\omega \tag{2.26b}$$

where φ_0 is the initial potential, d is the cross-sectional position starting from the center of the electrode gap and κ is the reciprocal of the Debye length. Note that this expression is only valid for regions within the electrodes because there are no counter ions in the electrode gaps. The velocity has a maximum at the electrode edges and decreases towards the center. [OHCN09]

2.1.7 Electrothermal Effects (Joule Heating)

Joule heating is caused by a current flow through the fluid according to the following expression:

$$k_T \nabla^2 T + \sigma_m E^2 = 0 \tag{2.27}$$

where k_T is the thermal conductivity and T the temperature. The unsteady and convective terms are neglected in this equation. An order of magnitude estimation of equation 2.27 can be done by

$$\Delta T \approx \frac{\sigma_m U^2}{2k_T} \tag{2.28}$$

where ΔT is the temperature increment [CRG+03]. The temperature field generates gradients of σ_m and ϵ_m. These gradients induce fluid motion acting on the suspended particles. For a detailed description of the force F_{ETE} refer to Oh *et al.* [OHCN09] and Lian and Wu [LW09].

2.2 Models of Cells

Biological cells are heterogeneous particles surrounded by a highly insulating membrane, which separates the cytoplasm from the exterior. The cytoplasm contains many smaller structures like the nucleus and other organelles, each surrounded by its own membrane. These layers, each with different electrical properties, can be represented by concentric shells.

2.2.1 Multi-Shell Model

Consider a spherical particle with a concentric shell (Fig. 2.3) exposed to a slightly non-uniform electric field. It can be shown [Jon95, p. 20ff] that the electric potential outside the particle is the same as that of the homogeneous sphere of permittivity $\underline{\epsilon}'_p$ given by Eq. 2.29.

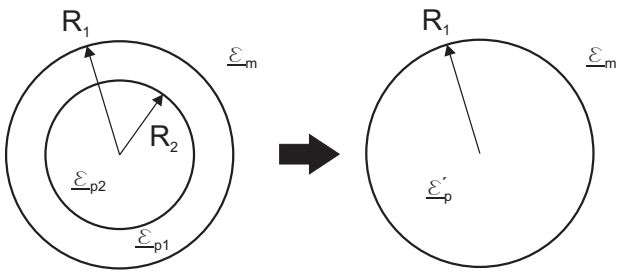

Figure 2.3: Layered spherical shell and equivalent homogeneous sphere [Jon03]

For a multi-shell model the innermost sphere and first shell are replaced by applying Eq. 2.29. Repeating this procedure, a N-shelled particle can be reduced to an equivalent homogeneous sphere.

$$\underline{\epsilon}'_p = \underline{\epsilon}_{p1} \frac{(\frac{R_1}{R_2})^3 + 2\frac{\underline{\epsilon}_{p2}-\underline{\epsilon}_{p1}}{\underline{\epsilon}_{p2}+2\underline{\epsilon}_{p1}}}{(\frac{R_1}{R_2})^3 - \frac{\underline{\epsilon}_{p2}-\underline{\epsilon}_{p1}}{\underline{\epsilon}_{p2}+2\underline{\epsilon}_{p1}}} \tag{2.29}$$

2.2.2 Thin-Shell Model

This model of a thin layered particle is useful for cells without an outer cell wall. Mammalian cells, for example, are surrounded by a membrane consisting of a lipid bilayer of a thickness of

$\delta = R1 - R2 << R1$. In this case the dielectric model can be simplified and the expression for the effective permittivity is [Jon03]

$$\underline{\epsilon}'_p = \frac{\underline{c}_m R \underline{\epsilon}_{p2}}{\underline{c}_m R + \underline{\epsilon}_{p2}} \tag{2.30a}$$

$$\underline{c}_m = c_m + g_m/j\omega. \tag{2.30b}$$

$c_m = \epsilon_{p1}/\delta$ and $g_m = \sigma_{p1}/\delta$ are the membrane capacitance and transconductance, respectively. Typical values of the membrane capacitance are about $10\,mF/m^2$. The transconductance is more variable and ranges from $10\,S/m^2$ to much higher values caused by opening membrane pores or channels [ST91].

2.3 DEP and ROT Spectra

Using the models described in the previous section, it is possible to simulate the DEP and ROT behaviour of cells. The spectra of a *Jurkat* cell according to the thin-shell model are shown in Fig. 2.4 for medium conductivities of $10\,mS/m$ and $40\,mS/m$, respectively. The model parameters are taken from Pethig and Talary [PT07]. As can be seen, the first crossover frequency is remarkably sensitive to the medium conductivity σ_m. It is shifted linearly towards higher frequencies with rising conductivity. The peaks of the ROT spectra related to $-\mathcal{I}[\underline{K}]$, correspond to the maximum rate of variation of $\mathcal{R}[\underline{K}]$.

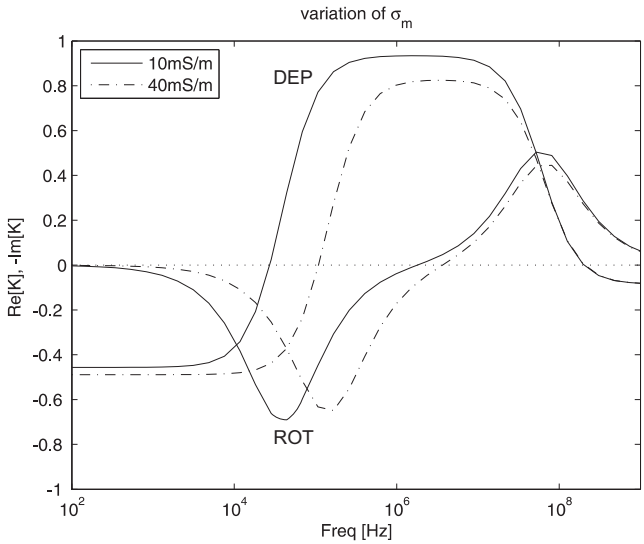

Figure 2.4: Simulated DEP and ROT response of a *Jurkat* cell using the thin-shell model with parameters: $c_m = 13.34\,mF/m^2$, $g_m = 70\,S/m^2$, $\sigma_{p2} = 0.7\,S/m$, $\epsilon_{p2} = 60\epsilon_0$, $\epsilon_m = 78\epsilon_0$, $\sigma_m = 40\,mS/m$ and $R = 6\mu m$ [PT07]

From measurements of both the DEP and ROT response, a unique solution for the model parameters c_m, g_m and ϵ_{p2} and σ_{p2} can be obtained [CGBP97]. Since the model shows different sensitivities to the parameters, the estimation accuracy varies. The influence of parameter variation on the spectra is illustrated in Fig. 2.5. Varying the cytoplasm permittivity ϵ_{p2} remains

the counter-field ROT peak unchanged, while altering the co-field peak (Fig. 2.5(a)). The cytoplasmic conductivity has a bigger influence on the first peak when its value is low (Fig. 2.5(b)). However, the sensitivity decreases dramatically when $\sigma_{p2} >> \sigma_m$, which usually is true for cells in DEP experiments.
Examining Figures 2.5(c) and 2.5(d) shows that altering c_m and g_m only affects the first ROT peak and the corresponding crossover frequency. This means that the behaviour of mammalian cells in the frequency range of interest solely is determined by the membrane properties.

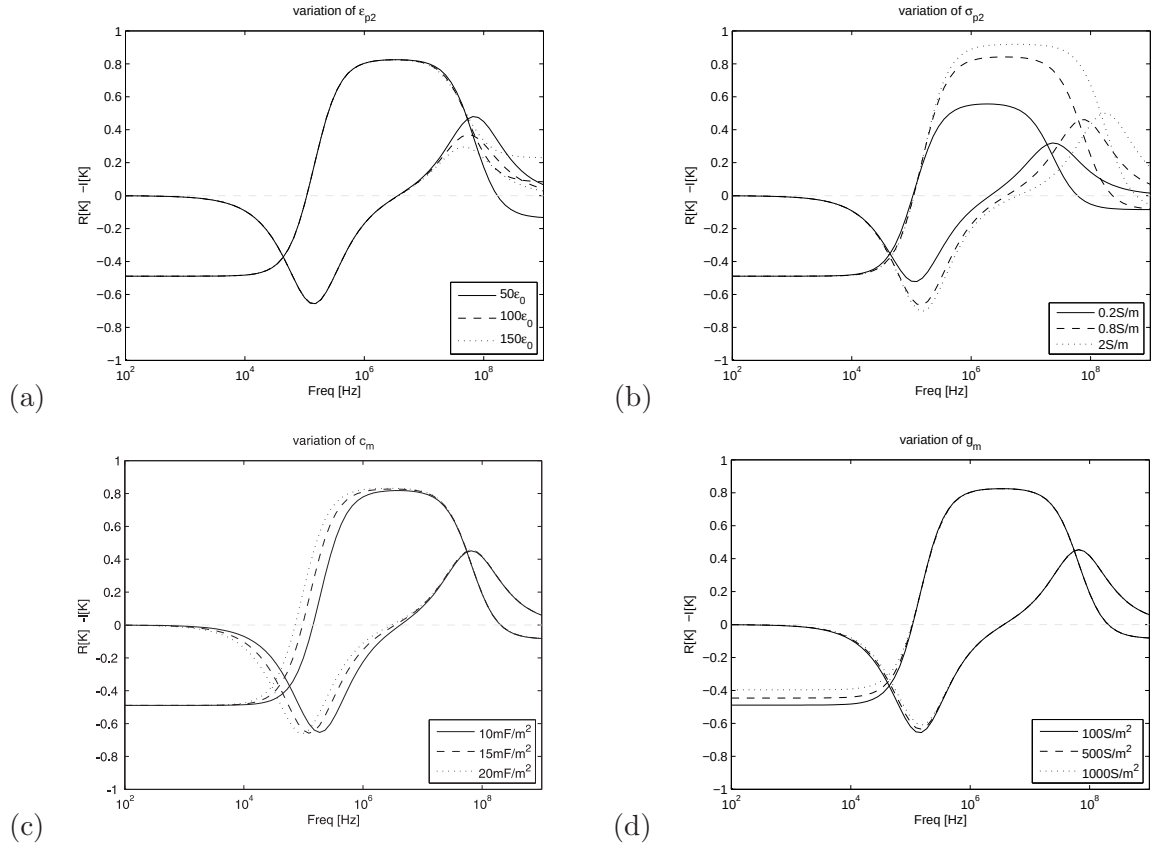

Figure 2.5: Thin-shell model sensitivity to parameter variation: (a) cytoplasm permittivity ϵ_{p2}. (b) cytoplasm conductivity σ_{p2}. (c) membrane capacitance c_m. (d) membrane conductance g_m.

Different mammalian cells have distinct values of the membrane capacitance c_m, which determines the crossover frequency of the DEP response. Fig. 2.6 depicts the simulated DEP response of two human cell lines. Note that the opposite sign of $R[\underline{K}]$ between the crossover frequencies result in oppositely directed DEP forces enabling separation of different cell lines. However, a separation by cell size ($F_{DEP} \propto R^3$) still is possible at other frequencies.

Walled cells like yeast and algae can be described by adding a second shell to the thin-shell model [HHPW92]. This adds another three parameters to the model, namely the dielectric properties of the wall ϵ_{p1} and σ_{p1} and its thickness δ_1. In Fig. 2.7 the spectra of a yeast cell according to the two-shell model is illustrated. In contrast to the thin-shell model the ROT peaks are unsymmetric because of the superposed impact of both shells. An equivalent analysis of parameter variation for the two-shell model is given in Appendix A.

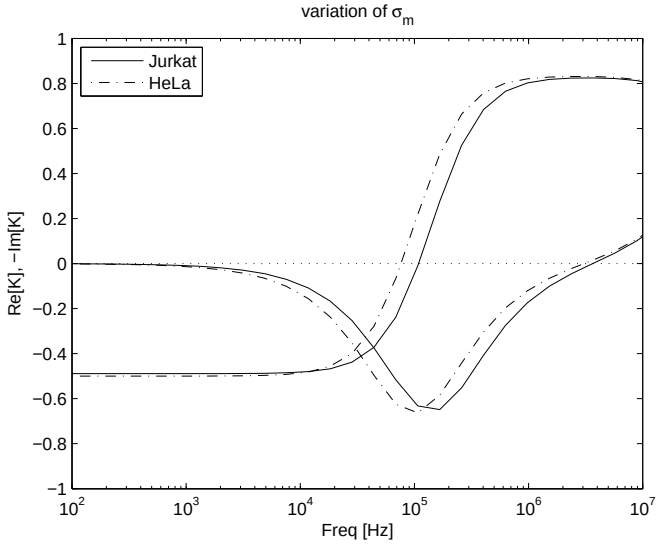

Figure 2.6: Simulated DEP and ROT response of human cell lines, parameters are taken from Pethig and Talary [PT07] and Asami *et al.* [AYT90] for *Jurkat* and *HeLa* cells, respectively.

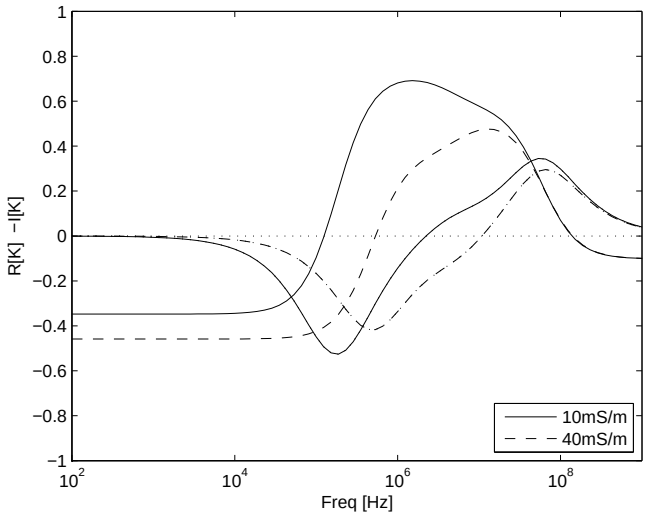

Figure 2.7: Simulated spectra for yeast according to the two-shell model. Parameters from Huang *et al.* [HHPW92].

3 Materials and Methods

To estimate the dielectric properties of different cell lines and to separate these cells, the DEP and ROT effects described in section 2 are utilized. Devices with different electrode geometries were fabricated for these purposes. In Section 3.1 the design considerations are discussed. To verify the principle of the different devices, simulations of the electric field distributions and cell trajectories were performed. The fabrication aspects are illustrated in Section 3.2, followed by the summary of measurement preparations and a description of the setup in Section 3.3.

3.1 Device Design

The used device holder and the printed circuit boards were designed and fabricated within a previous work [Avi07]. For this reason the size of the devices and the number and position of inlets were fixed. The dimensions of a single DEP device are depicted in Fig. 3.1.

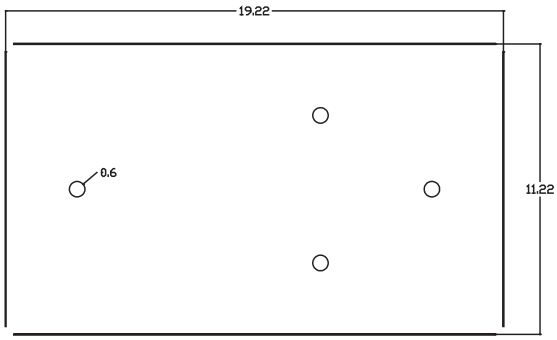

Figure 3.1: Dimensions of a single DEP device [mm]

The factor ∇E_{rms}^2 of the time-averaged DEP force dimensionally is V^2/m^3. Thus a sensitivity of the DEP force can be expressed by

$$|\mathbf{F}_{DEP}| \propto U^2/l^3 \tag{3.1}$$

where U is the applied voltage and l is the characteristic dimension of the electrodes [BB79]. Accordingly, downscaling of the electrode dimension, e.g. by a factor of 100, enables a voltage reduction by a factor of 1000 for the same value of the DEP force. However, the DEP force strongly depends upon the electrode geometry. Therefore, simulations are necessary to get closer analyses of the different electrode geometries.

3.1.1 Simulations of DEP Devices

Numerical simulations of the dielectrophoretic force and the fluid flow were performed with the finite element software *COMSOL Multiphysics* for each device. These results were used in a *MATLAB* script to calculate cell trajectories.

COMSOL provides a graphical editor for creating 3D models of the DEP devices. The electric field distribution, from which the dielectrophoretic force F_{DEP} is derived, is calculated using the *Quasi-Static AC/DC Application Mode*. Only a short part of the continuous-separation devices is simulated and repeated in a loop in *MATLAB*. The simulation parameters, defining the device properties, are summarized in Table 3.1.

Boundary Settings		
Description	Boundary Condition	Value
electrode	electric potential	$1V$
counter electrode	ground	predefined
channel wall	electric insulation	predefined

Subdomain Settings	
Name	Value
ϵ_m	$78\epsilon_0$
σ_m	0

Subdomain Expressions	
Name	Value
dE_X	$diff(normE^2_{emqvw}, x)$
dE_Y	$diff(normE^2_{emqvw}, y)$
dE_Z	$diff(normE^2_{emqvw}, z)$

Table 3.1: Parameters of the electric field simulation

To move the cells through the separation channel, a fluid flow is needed that is simulated with the *Incompressible Navier-Stokes MEMS Application Mode*. The solution of this simulation gives the medium velocity v_m within the channel. The required parameters are shown in Table 3.2.

Boundary Settings		
Boundary Type	Boundary Condition	Value
Inlet	Laminar inflow	$V_0 = 1 \cdot 10^{-9}/60 m^3/s$ $(1\mu l/min)$
Wall	No slip	-
Outlet	Pressure, no viscous stress	$p = 0Pa$

Subdomain Settings	
Name	Value
ρ	$1.05 \cdot 10^3 kg/m^3$
η	$1.37\, mPas$

Table 3.2: Parameters of the fluid velocity simulation

To estimate a cell trajectory, the cell velocity v_p in a certain point is calculated by $F_{DEP}(x,y,z) = F_{scale}K_{cell}\nabla E^2_{rms}(x,y,z)$ and $v_p(x,y,z) = F_{DEP}(x,y,z)/(6\pi\eta R) + v_m(x,y,z)$. With v_p in the current point and the time step ΔT the trajectory is calculated point by point through $pos(i+1,:) = pos(i,:) + v_p\Delta T$. See *trajectory.m* in Appendix C for details.

3.1.2 Devices

The design considerations for each electrode geometry are described below along with schematic diagrams and simulation results. For details of the fabricated masks refer to Appendix B.

3.1.2.1 Quadrupoles

Quadrupolar electrodes are commonly used to estimate the DEP crossover frequency and the ROT spectrum [HHPW92, PJS+05]. The electrodes for DEP experiments are designed according the polynomial geometry described by Huang and Pethig [HP91]. Fig. 3.2 shows the electric field distribution of these electrodes at $15\,\mu m$ height, a voltage of $1V$ and an electrode distance of $d_t = 400\,\mu m$. In the middle of the four electrodes an isolated field minimum occurs. Whereas cells are collected in this region by nDEP forces, they are directed towards the electrodes' edges by pDEP. Note that there are additional electric field minimas at the center of each electrode. Since the field gradient is larger in this direction than towards the center, cells located at the edges are moved outwards when nDEP is present.

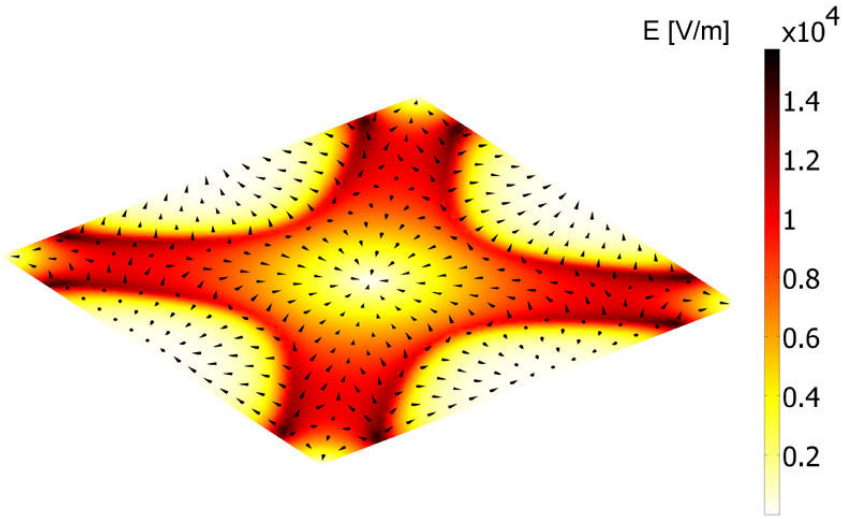

Figure 3.2: Simulation of polynomial electrodes; Surface plot: Electric field[V/m], Arrows: nDEP force ($h = 15\,\mu m, U = 1\,V, d_t = 400\,\mu m$)

The polynomial, quadrupolar electrodes were fabricated with a tip to tip distance of $d_t = 240\,\mu m$, $d_t = 400\,\mu m$ and $d_t = 600\,\mu m$. According to the scaling law Eq. 3.1, this makes it easier to adjust the DEP force to varying cell sizes within a given range of voltage supply.

The devices for ROT experiments were fabricated with rectangular electrodes of distances of $d_t = 615\,\mu m$ and $d_t = 720\,\mu m$. The electrode arrangement with the excitation voltage to create a rotating electric field is shown in Fig. 3.3.

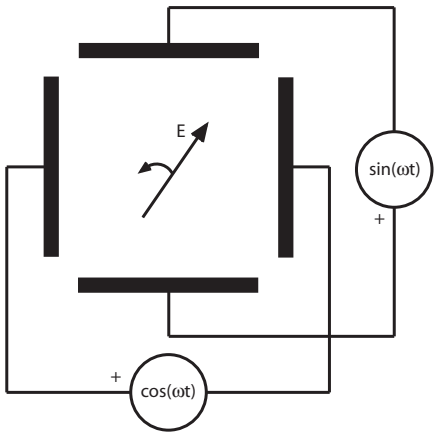

Figure 3.3: Excitation voltage to create a rotating electric field

3.1.2.2 Interdigitated, Castellated Electrodes

This electrode geometry has been used by others for a variety of dielectrophoresis studies [PHWB92, GRM00]. It was found that the interdigitated, castellated electrodes show the possibility of separate collection of cells by pDEP and nDEP forces. The schematic Fig. 3.4(a) shows the electrode design as well as the collection of different cells. The electrode dimensions are equally chosen to them used with cells by Pethig*et al.* [PHWB92, PJS+05], but the gap between the electrodes is reduced to $40\,\mu m$ for reasons described below.

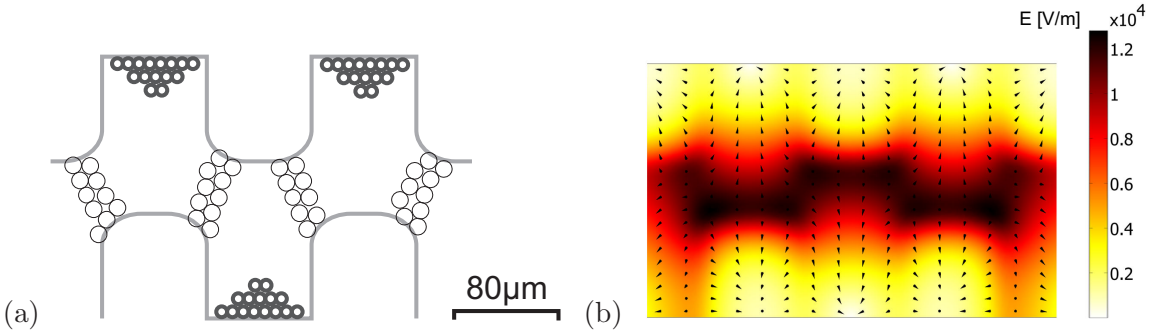

Figure 3.4: Interdigitated, castellated electrodes: (a) Design and particle collection for pDEP between the electrodes and nDEP at the electrode bays (cp. [PHWB92]). (b) Electric field simulation ($h = 15\,\mu m, U = 1\,V$).

Comparing Fig. 3.4(a) to the electric field distribution in Fig. 3.4(b) shows that the cell aggregation under the influence of pDEP corresponds to the regions of the highest electric field. The arrows in Fig. 3.4(b) indicate the cell paths for negative DEP. Note that the direction of the force alternates from electrode to electrode in the high-field region between the electrodes. This is an important finding if this design is used for a continuous separation where a fluid flow from left to right is introduced. Trajectory simulations showed that a cell entering this region is not moved outwards by nDEP force if the distance of the electrodes is too big compared to cell size. Fig. 3.5 illustrates the trajectories of cells ($R = 6\,\mu m$) for different starting positions and values of the Clausius-Mosotti factor K of -0.3 and 0.3, respectively. The red lines indicate the trajectories

of cells under pDEP influence. These cells are forced towards the flattened electrode edges and move along them to the outlet. Cells for which nDEP is present are repelled from the high field regions towards the channel wall (dotted, blue lines). It can be seen that the deflection of cells by nDEP forces is less effective because they are lifted above the electrodes, where the electric field decreases.

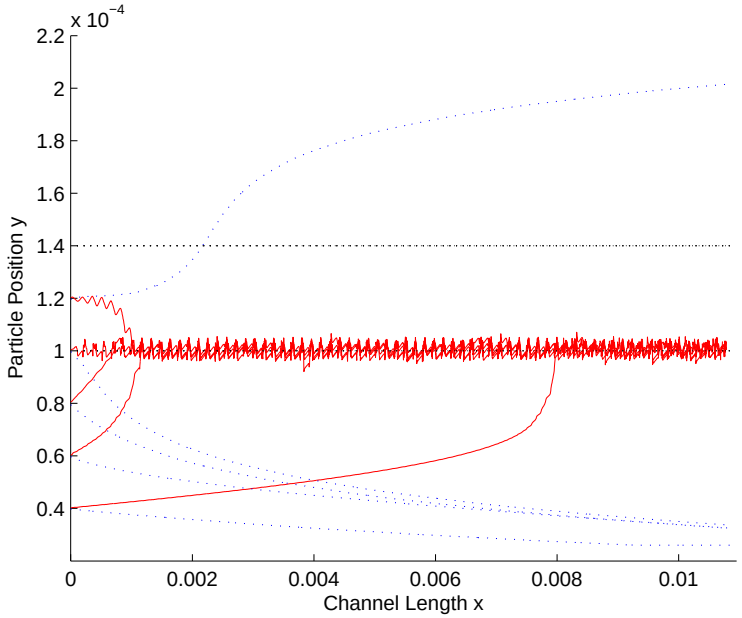

Figure 3.5: Interdigitated, castellated electrodes: Cell trajectories for different starting positions ($h = 15\,\mu m$). Simulation parameters: $K_{red} = 0.3$, $K_{blue} = -0.3$, $R = 6\,\mu m$, $U = 2\,V$, $v = 0.2\,\mu l/min$, $\Delta t = 8\,ms$

3.1.2.3 Interdigitated, elliptical Electrodes

As described before, the interdigitated, castellated electrodes (Section 3.1.2.2) have regions where the DEP force direction changes along the microchannel. To avoid this phenomena, the electrodes of the interdigitated, elliptical design are moved together. The arrows in Fig. 3.6, indicating negative DEP force, show the well directed force from the center towards the channel walls. Local field maxima that occur on sharp corners are avoided by the elliptical shape.

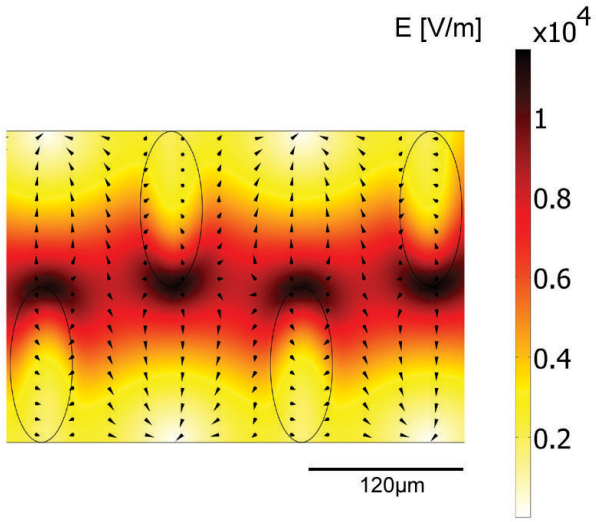

Figure 3.6: Electric field distribution of interdigitated, elliptical electrodes ($U = 1\,V$, $h = 15\,\mu m$)

The interdigitated, elliptical electrodes can be used for a continuous cell separation by utilizing pDEP and nDEP forces. A corresponding trajectory simulation is depicted in Fig. 3.7. If trapping of cells undergoing pDEP can be avoided, the simulation suggests a high separation efficiency. Due to the limited size of the finite elements and the time steps in combination with the high force values in the central region the pDEP trajectories appear quite noisy.

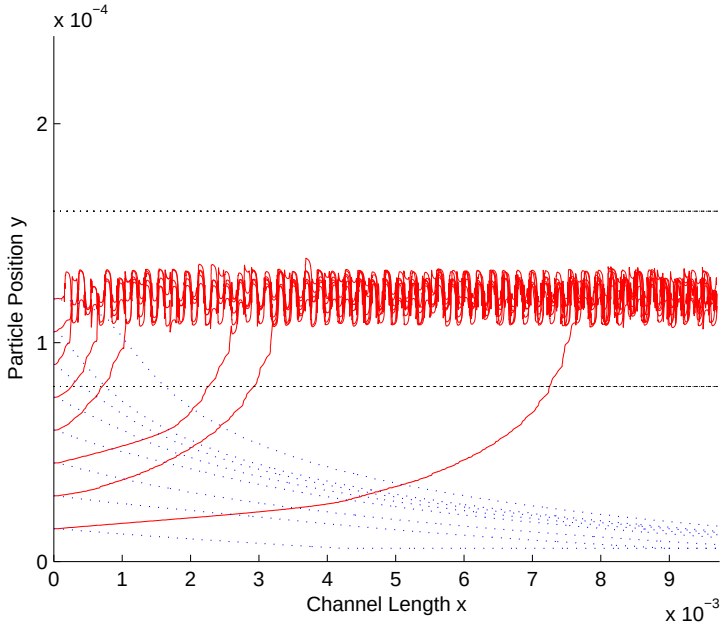

Figure 3.7: Interdigitated, elliptical electrodes: Cell trajectories for different starting positions ($h = 15\,\mu m$). Simulation parameters: $K_{red} = 0.3$, $K_{blue} = -0.3$, $R = 6\,\mu m$, $U = 3\,V$, $v = 0.2\,\mu l/min$, $\Delta t = 10\,ms$

3.1.2.4 Triangular Electrodes

Gradually sloped electrodes are a classical approach to produce a non-uniform electric field. It was shown that plane electrodes have a better performance than strip electrodes [NV03]. Aligning them perpendicularly to the flow direction increases the number of DEP actuators (Fig. 3.8). As can be seen, a force perpendicular to the flow is only produced in the electrode gaps. For this reason the area of the the electrodes is kept small compared to the gaps, maximizing the time a cell is subjected to this force vector. On the other hand, the supply voltage has to be increased compared to the other devices, caused by the larger distance between the electrodes.

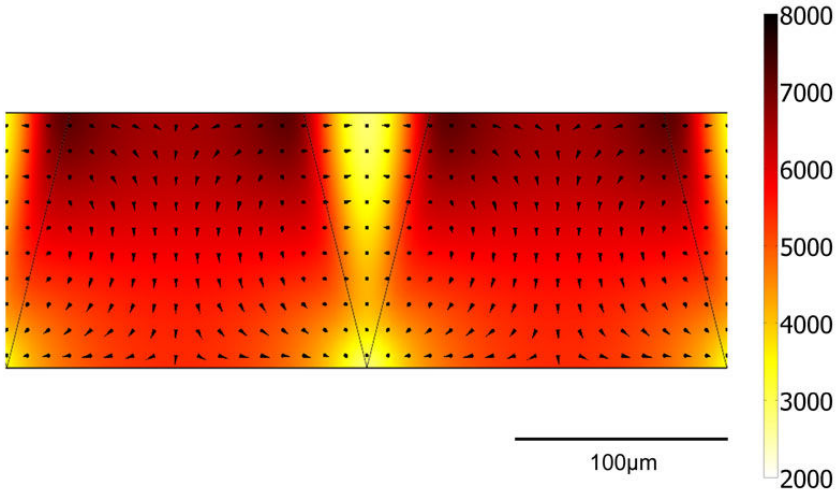

Figure 3.8: Electric field distribution of interdigitated, elliptical electrodes ($U = 1\,V$, $h = 15\,\mu m$)

As well as the previous described devices, the triangular electrodes can be used for a separation by pDEP and nDEP forces. Another possibility is to separate cells by nDEP forces only. In this case the sample stream is hydrodynamically focused to the high-field side of the channel. After this, the cells are deflected by nDEP forces. A separation due to differences of $\mathcal{R}(\underline{K})$, but more important by cell size, is possible. This is a popular approach, applied by others to separate polystyrene particles of pretty different radii [CP05, CCH+09]. In Fig. 3.9 the simulation results of nDEP based cell separation is shown. The assumed radii of $6\,\mu m$ and $1.2\,\mu m$ represent the separation of T-lymphocytes and bacteria. Note, that the quality of sample focusing highly affects the separation efficiency.

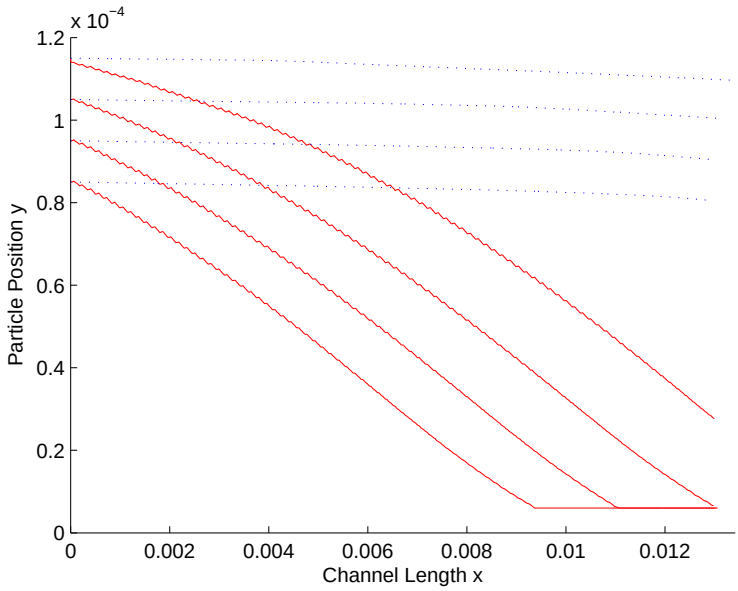

Figure 3.9: Triangular electrodes: Cell trajectories for nDEP based separation ($h = 15\,\mu m$). Simulation parameters: $K = -0.4$, $R_{red} = 6\,\mu m$, $R_{blue} = 1.2\,\mu m$, $U = 5\,V$, $v = 0.15\,\mu l/min$, $\Delta t = 10\,ms$

3.1.2.5 Travelling Wave Devices

Devices for travelling wave dielectrophoresis are designed in two electrode configurations. The spiral electrode design, shown in Fig. 3.10(a), is commonly used to perform basic travelling wave studies. Four concentric electrodes are energized by 90° phase-shifted signals (0°, 90°, 180°, 270°), which produce an electric field with a travelling component. The spatially dependent phase results in a horizontal force directed towards the center of the spiral or away. As obtained by the first term of Eq. 2.22, an additional DEP force component is produced by the non-uniform field in the vertical dimension. This component levitates the cells or attracts them to the electrodes. Gascoyne *et al.* have shown the capability of the spiral electrodes to concentrate rare cells in the center [GMM+02].

The advantage of the spiral design is that there are only four bonding pads in contrast to the parallel electrodes (Fig. 3.10(b)), where every single electrode has to be bonded. On the other hand, cells once collected at the center of the spiral cannot be moved elsewhere. With the parallel electrodes, however, a continuous operation is possible. Cells entering the device from the left can be directed to any desired y-position by changing the phase sequence of the electrodes. Therefore, this design permits accurate output switching.

The electrodes of both designs were fabricated according to Wang *et al.* [WHW+97] with equal electrode widths and gaps of 20 μm to ensure that the cells are subjected to a continuous travelling field.

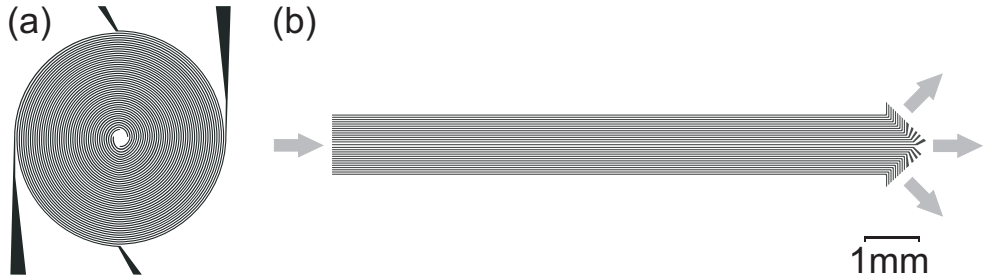

Figure 3.10: Travelling wave devices: (a) Spiral electrodes. (b) Parallel electrodes.

3.2 Fabrication of DEP Devices

A 4-inch, 500 μm thick glass wafer is used as the base material of the devices. The microfluidic channels are formed within a PDMS cover that adheres on the glass. Platinum, evaporated on the glass surface, is used for the electrodes. For better visibility of cells, a reflective titan layer is deposited on the underside.
Masks for the fabrication of the electrode structures and the channels, drawn in *Autocad 2004*, are depicted in Appedix B. The process steps are outlined in the following (Fig. 3.11).

Structuring of the electrodes using a lift-off-process:

(a) Spin coating of an image reversal photoresist (*AZ 5214*) on the glass wafer, pre-baking at 107°C for 5 min on a hotplate and UV exposure through the mask.

(b) Reversal-bake at 120°C for 2 min, flood exposure and development by a solvent.

(c) Vapour deposition of a 50 nm undercoating titanium layer and 100 nm platinum.

(d) Removal of the photoresist with the covering metal layer.

Fabrication of the channels in PDMS:

(e) Spin coating of SU-8 2050 photoresist on a silicon wafer with an undercoating titanium layer (500 rpm - 16 s, 2000 rpm - 15 s, 3200 rpm - 40 s). This gives a layer thickness of approximately 30 μm.

(f) Drying (soft-bake) at 95°C on a hotplate for 45 min and exposure with a UV mask aligner.

(g) Post exposure bake at 90°C for 30 min to crosslink the exposed resist.

(h) Dissolving of the unexposed resist by a PGMEA solvent and hard-bake at 200°C for 1 h.

(i) A PDMS composite silicone (*Sylgard 184*) is vacuum outgassed and poured over the SU-8 mold. Curing of the PDMS layer is done at 70°C for 1 h. The top surface is flattened with a clamped foil.

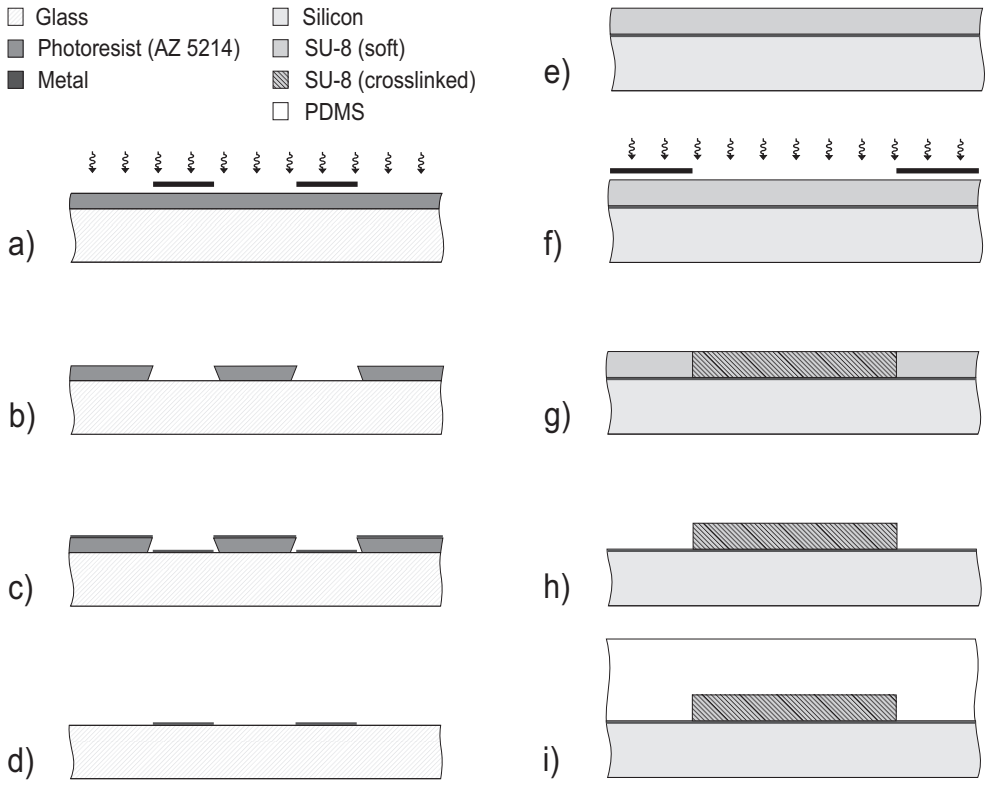

Figure 3.11: Process steps of DEP device fabrication

After these process steps the inlets are drilled with a diameter of 0.6 mm and the wafer is cut along the marks into single devices. The PDMS can be cut easily into pieces with a scalpel. For proper alignment of the microchannel and the electrodes, marks are provided on the glass and the PDMS cover. Before assembling the device, the glass and the channel are cleaned with ethanol, rinsed with DI water and dried with nitrogen gas. The PDMS adheres well on the glass surface without need of any further fixation. A finished DEP device is shown in Fig. 3.12.

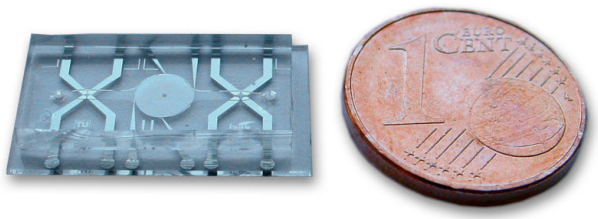

Figure 3.12: Finished, assembled device compared to 1 cent

3.3 Measurement Preparations, Setup and Postprocessing

3.3.1 DEP Medium

To reduce the high conductivity of the cell culture media and to compensate for osmotic pressure, the cells are suspended in a sucrose-dextrose solution in deionized water. To reduce sedimentation during the experiments, the DEP medium density is adjusted by adding sucrose to deionized water. Additionally dextrose is added as a metabolic energy source. Table 3.3 shows the medium mixture for different measurements. The density and viscosity values are taken for sucrose in water from Lide [Lid98]. In the range of interest the values can be approximated by: $\rho = 0.004103 * mass[\%] + 0.9972$ and $\eta = 3.51e-005 * mass^3 + 0.0003147 * mass^2 + 0.02688 * mass + 0.9998$. Calculating once again the sedimentation velocity according to Section 2.1.5 reduces it to a value of $0.98\,\mu m/s$ for the same cell properties in a medium with 8.6% sucrose and 0.3% dextrose. An exact match of the densities is not desired, because this makes harvesting by centrifugation inefficient. The conductivity of the medium is adjusted by adding phosphate buffered saline (PBS).

DEP medium				
Cell Type	Sucrose	Dextrose	Density $[g/cm^3]$	η $[mPa\,s]$
T-lymphocytes	8.6 %	0.3 %	1.0339	1.289
T-lymphocytes + bacteria, algae	10 %	1 %	1.042	1.38
Yeast, bacteria, polystyrene beads	12 %	2 %	1.055	1.534

Table 3.3: DEP medium; Sucrose and dextrose in water solution [%w/w]

3.3.2 Cell Types

To test the separation efficiency under different circumstances, cells of varying size and morphology are utilized for DEP measurements. Beside human cell lines and bacteria, yeast and algae cultures serve as appropriate model cells. Yeast and algae have the advantages that they are readily available, easy to handle and durable in storage.

T-lymphocytes are cultivated at 37°C in a DMEM medium containing $4.5\,g/l$ glucose, $2\,mM$ L-glutamine, 10 % fetal calf serum and antibiotics ($100\,units/ml$ penicillin, $100\,\mu g/ml$ streptomycin and $0.25\,\mu g/ml$ amphotericin B). They are available in types of *Jurkat* and *T2-lymphocytes* and are kindly provided by *W. Witarsky, Institute of Virology, Slovak Academy of Sciences*.

Baker's yeast (*Saccharomyces cerevisiae*) is obtained in fresh, refrigerated packets from a supermarket. Just before the measurements a small piece is suspended in 10 ml DEP medium and mixed. After 5 min of sedimentation of large cell clusters, which would cause clogging of the channel, 1 ml of the mix is used for sample preparation.

Lactobacillus casei bacteria are provided by the *Austrian Institute of Technology* to prove the separation of bacteria from cells. This is interesting for checking bacterial contamination of blood preservations. *L. casei* are rod-shaped with a length up to $4\,\mu m$, but often form short chains of two or three.

Nannochloropsis sp. are small unicellular marine algae, usually cultivated for marine aquaristic purposes. They are obtained from the *Korallenriffcenter* in sea water medium and can be stored refrigerated for at least a week.

Isochyris galbana are marine algae as well, but flagellated and larger than *Nannochloropsis sp.* Furthermore they do not have a distinct cell wall, whereby they are more fragile. They are kindly provided by *Dr. D. Abed-Navandi, Haus des Meeres.*

Oocystis sp. are fresh water algae of the form of oblate sphericals with a size of $20-35\,\mu m$ x $10-20\,\mu m$. One to four cells are surrounded by a thick cell wall (Fig. 3.13(e)). They are provided by *Dr. D. Abed-Navandi, Haus des Meeres* as well.

The different cell types are shown in Fig. 3.13 and their average diameters are given in Table 3.4.

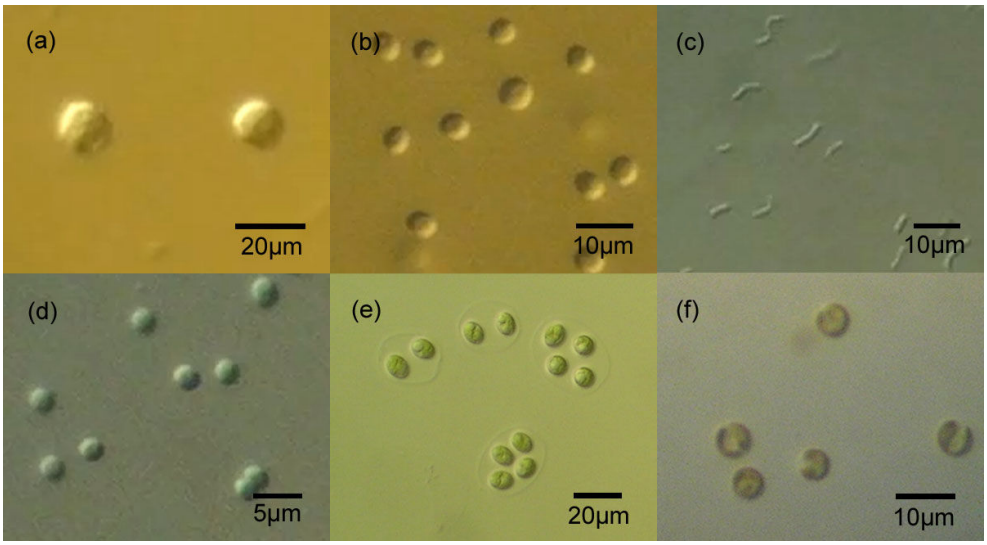

Figure 3.13: Used cells: (a) T-lymphocytes. (b) *Saccharomyces cerevisiae.* (c) *Lactobacillus casei.* (d) *Nannochloropsis sp.* (e) *Oocystis sp.* (f) *Isochrysis galbana.*

Name	Type	Average Cell Size
T-lymphocytes	human cells	$14\,\mu m$
Saccharomyces cerevisiae	baker's yeast	$4.72\,\mu m$
Lactobacillus casei	bacteria	1 x $3\,\mu m$
Nannochloropsis sp.	marine algae	$2.7\,\mu m$
Isochrysis galbana	marine algae	$5.66\,\mu m$
Oocystis sp.	fresh water algae	$20-35\,\mu m$ x $10-20\,\mu m$

Table 3.4: Cell types used in DEP experiments

3.3.3 Sample Preparation

All cell types are treated equally in this preparation step to achieve comparable results. The cells are harvested by centrifugation and the cultivation medium is removed. Afterwards they are

washed twice in 5 ml DEP medium of the desired conductivity. This step is important to remove all culture medium components, which would influence the DEP medium conductivity.

3.3.4 Measurement Setup

The overall setup for the measurements is shown in Fig. 3.14. Each chip is glued on a printed circuit board (PCB) with a rectangular opening to access the inlets of the chip. For the voltage supply of the electrodes thin copper wires are soldered on the bonding pads of the chip and the PCB. AC power is supplied by an *Agilent 33220A* signal generator. For ROT and TWD experiments a second generator is used. In this case the two signals are 90° phase-shifted and secondary decoupled by two broadband transducers. Unfortunately the upper frequency boundary decreases from 20MHz to about 3MHz due to the transducers.
Basic measurements of crossover frequencies and ROT spectra are performed without an external flow. In this case the device holder and the syringe pumps are not needed. The sample is directly filled into the device by a syringe with a silicone tip. To avoid flow disturbance during the measurements, the inlets are sealed with a piece of PDMS.
For continuous separation experiments the sample is pumped through the device by a *KD Scientific 200P* syringe pump. Optionally, a second pump is used for a sheath flow. The tubes of the device holder are connected to the syringes and filled with DEP medium before the measurements. The sample suspension is introduced into the inlet-tube via the O-ring of the holder while the syringe pump is operated in withdrawal mode.
A droplet of ethanol is pipetted on top of one inlet of the device and fills it by capillary action. The device is rinsed with DEP medium afterwards without introducing air bubbles. Screwing the PCB onto the holder finalizes the preparations for experiments. The measurement results are captured by a *Samsung VP-HMX20C* camcorder mounted on a *Carl Zeiss Axiotron* microscope.

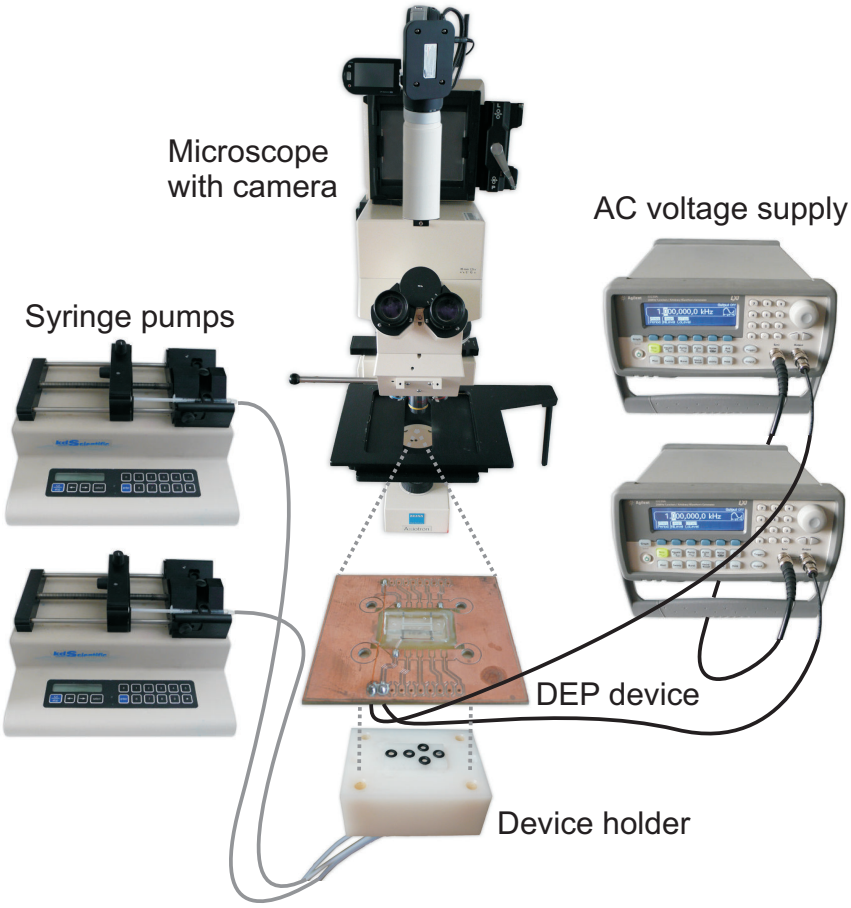

Figure 3.14: Measurement Setup

3.3.5 Data Analysis

3.3.5.1 Determination of DEP Crossover Frequency

Crossover frequency measurements are conducted with the polynomial, quadrupolar electrode geometry described in Section 3.1.2.1. Voltages of $2 - 6\,V_{rms}$ are used, depending on the cell type and the electrode distance d_t. The electric field is applied at a frequency at which nDEP is expected. As soon as the direction of cell motion is determined, the frequency is switched to a value where pDEP is present. Afterwards the frequency is increased in the nDEP and decreased in the pDEP band until the DEP force is observed to be zero. Crossover frequency measurements have the advantage of speed over ROT experiments, as they can be completed within a minute. On the other hand the exact value of the crossover frequency is difficult to detect because cell motion is very slow around f_{C0}.

3.3.5.2 ROT Data Interpretation

To determine the rotational velocity of cells, single images are extracted from the captured video files using a freeware framegrabber (*ImageGrab 4.2*). From these images the rotations per frames

are easily observable. Only cells are considered that are located close to the center of the electrodes. The distance between cells should be at least four cell diameters to avoid an influence of the dipolar field of neighbouring cells [GBW95].

ROT spectra are non-linear functions of the dielectric parameters of the cell and the medium given by

$$f_{ROT}(\omega) = k_R \mathcal{I}\left[\frac{\underline{\epsilon}_p' - \underline{\epsilon}_m}{\underline{\epsilon}_p' + 2\underline{\epsilon}_m}\right] \tag{3.2}$$

where k_R is a scaling factor related to $\epsilon_m E_0^2/2\eta$. Usually this factor is unknown because the local electric field strength and frictional forces are uncertain [GBW95]. Unknown parameters are derived by an iterative optimization procedure. This procedure uses the Nelder-Mead simplex optimization provided by *MATLAB* to minimize the residual error:

$$Min_{parameters}\left\{\sum_i [f_{ROTexp}(i) - f_{model}(i)]^2\right\}. \tag{3.3}$$

Applying the thin-shell model of Section 2.2.2, the ROT spectrum is a function of five unknowns: $c_m, g_m, \epsilon_{p2}, \sigma_{p2}$ and the scaling factor k_R. The analysis of Section 2.3 shows that each ROT peak is determined independently by two variables. Therefore, a complete ROT spectrum allows the accurate derivation of four and only four parameters. Since the maximum frequency f_{max} of ROT experiments is about $3\,MHz$, the cofield rotation peak is not detectable. Thus, the sensitivity of the ROT spectrum towards ϵ_{p2} and σ_{p2} is very low and their estimation is uncertain [GBW95]. For this reason, the cytoplasmic properties ϵ_{p2} and σ_{p2} are fixed in the optimization and only c_m, g_m and k_R are estimated. By providing crossover frequency data an accurate estimation of the remaining three parameters can be done. In this case the error function to be minimized is

$$Min_{parameters}\left\{\sum_i [f_{ROTexp}(i) - f_{model}(i)]^2 + W\mathcal{R}[\underline{K}_{model}(f_{C0})]^2\right\}. \tag{3.4}$$

where the weighting factor W determines the relative emphasis on ROT and DEP data. Refer to the *MATLAB* code in Appendix D for details.

For yeast and bacteria a two-shell model is used for the optimization. The dielectric properties ϵ_{p1} and σ_{p1} of the cell wall and its thickness δ_1 have to be determined additionally. To achieve an accurate parameter estimation the cell wall permittivity ϵ_{p1}, the thickness δ_1 and g_m are taken from literature.

3.3.5.3 Separation Analysis

To determine the separation efficiency of the different devices, position detection of hundreds of cells in a short time is required. The channel is widened in the detection zone to slow the cells down (Fig. 3.15(a)). A detection window at the outlet is defined in which the y-position of a passing cell is determined. The presence of a cell is detected by the difference of the actual video frame and a background calculated from two preceding frames. A custom made software based on *Intel OpenCV* is used, which was developed within a previous work. To avoid multiple counting,

a tracking algorithm uniquely identifies any single cell (Fig. 3.15(b)). The obtained position data is used to plot histograms of the cell distributions. Threshold values of particle area allow the selective detection of one cell type in a mix. The limitation of the selective cell detection is also observable in Fig. 3.15(b). The yeast cells are more strongly deflected and lifted by nDEP forces than *Nannochloropsis sp.* cells. Because *Nannochloropsis sp.* move faster and appear elongated in the single video frames, the discrimination by area is difficult for these small cell types .

(a) 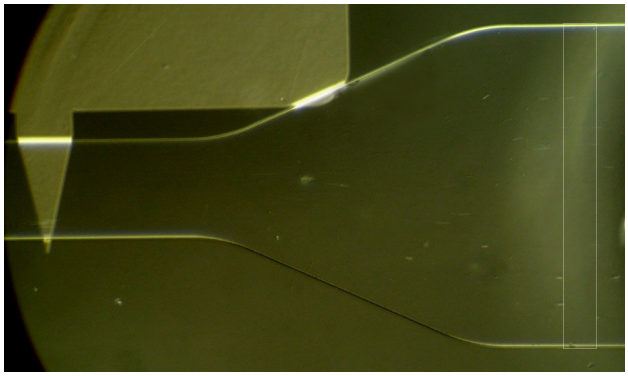 (b) 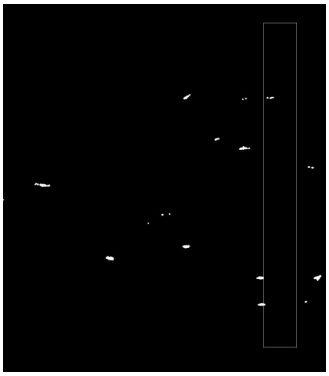

Figure 3.15: Video analysis of cell separation. (a) Separation zone with detection window. (b)Image processing for position detection.

4 Results and Discussion

The experimental results of cell characterization and separation measurements are presented in this chapter. Conditions for a safe operation environment are described in Section 4.1. Experimentally obtained DEP and ROT spectra and the estimated properties for the different cell types are illustrated (4.2). The derived values are used in simulations to choose an appropriate separation mode for cell mixtures. The results of separation experiments are presented in Section 4.3.

4.1 Operating Conditions and External Effects

The major side effects of DEP measurements are cell sedimentation (already discussed in Section 3.3.1), AC electro osmosis (ACEO) and electrothermal effects (ETE). Since ACEO and ETE depend upon the medium conductivity and the applied frequency, experiments were carried out to analyze their impact at medium conductivities of $0.4\,mS/m$ and $40\,mS/m$. The electrohydrodynamic effects give rise to fluid motion, which drags the cells along. According to Eq. 2.23 the drag force scales linearly with cell radius. In order to keep DEP forces ($\propto R^3$) low, the small *Nannochloropsis sp.* cells ($R = 1.35\,\mu m$) were used in these experiments.

At frequencies well above the crossover frequency the cells collected at the electrodes' edges (Fig. 4.1(a)). No remarkable difference was observed between the two medium conductivities. When the frequency was switched to the nDEP band, only at $40\,mS/m$, $f = 10\,kHz$ a well defined cell collection occurred (Fig. 4.1(b)). In the frequency range $100\,Hz - 30\,kHz$ the DEP effects at both medium conductivities were accompanied by cell motion induced by AC electroosmosis.

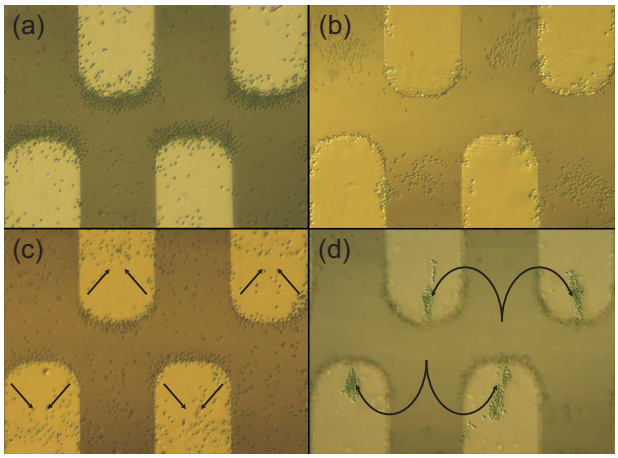

Figure 4.1: Behaviour of *Nannochlorpsis sp.* under varying circumstances: (a) pDEP collection at 5 V (50 kHz at 0.4 mS/m, 5 MHz at 40 mS/m). (b) nDEP collection at 5 V, 10 kHz and 40 mS/m. (c) AC electroosmosis 5V (5 kHz at 0.4 mS/m and 40 mS/m). (d) Circular motion 10V (5 kHz at 0.4 mS/m and 40 mS/m).

As shown in Fig. 4.1(c) the cells moved from the surrounding area of the electrodes across the electrodes' edges and towards the center. If the frequency was further decreased or the voltage was increased, a wide range circular motion was dominant, which leaded to cell aggregation illustrated in Fig. 4.1(d). Time-periodic faradaic reactions produced coions at the electrodes instead of attracting counterions. As a result, the electroosmotic flow was in the opposite direction of double-layer induced ACEO [LZW+04].
Electrothermal effects did not seem to play an important role compared to the strong pDEP effects at high frequencies. For this reason additional measurements were performed using $4\,\mu m$ polystyrene particles at $0.4\,mS/m$ and $125\,mS/m$.

Polystyrene particles exhibit a constant, negative value of $\mathcal{R}(\underline{K})$ over the entire spectrum. However, nDEP was dominant in the $100\,kHz$ range only. Particles were collected in the electrode bays with no obvious difference for both medium conductivities (Fig. 4.2(a)). AC Electroosmosis decreases with rising medium conductivity [Baz08] and vanishes for a conductivity above $85\,mS/m$ [Wu08]. Since the particle formation of Fig. 4.2(b) was more clearly observable at $125\,mS/m$, electrothermal effects (ETE) have to account for this effect. At $1\,MHz, 10\,V$ and $0.4\,mS/m$ the particles collected at a different stable position (Fig. 4.2(c)) . ACEO again is supposed to be less important at such high frequencies [OHCN09]. On the other hand, ETE are commonly treated as frequency-independent, which was not observed for this particle accumulation. However, it is difficult to distinguish both effects, because when no surface heating is included, ACEO and ETE result in forces in the same direction [LW09]. When the voltage was raised to values above $10\,V$, faradaic currents arose again at low frequencies and produced gas bubbles at the electrodes (Fig.4.2(d)).
The observed electrokinetic effects are complex and have not been yet formulated in a complete theoretical model. In recent years considerable research has been done to utilize these effects for micropumps and micromixers (e.g. [KL09], [LZW+04], [UT06]).

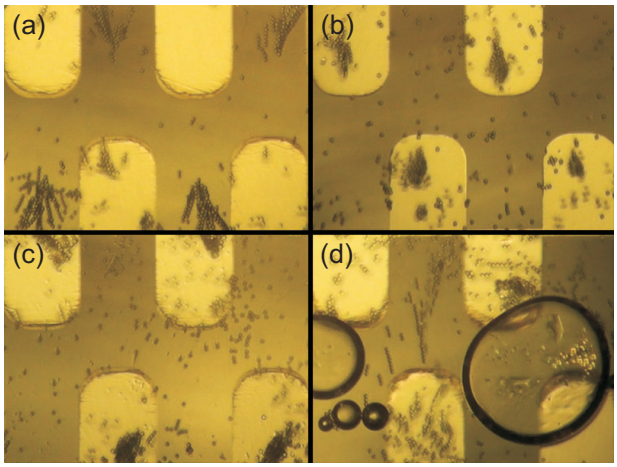

Figure 4.2: Behaviour of $4\mu m$ polystyrene particles: (a) nDEP collection, $100\,kHz$, $10\,V$. (b) Particle collection on the electrodes at $5\,kHz$, $5\,V$ and $125\,mS/m$. (c) Particle collection on the electrodes at $1\,MHz$, $10\,V$ and $0.4\,mS/m$. (d) Bubble formation at $5\,kHz$, $14\,V$, $0.4\,mS/m$.

To sum up, these results show that DEP clearly predominates the behaviour of cells above $100\,kHz$. A medium conductivity below $100\,mS/m$ at which the crossover frequency is in this range should give best results. Additionally, the applied voltage for this device should be well below $10\,V$ to reduce the influences of electrothermal effects and faradaic currents. Another voltage limiting factor is the fact that cells can burst by high electric fields. Menachery and Pethig [MP05] suggest to keep electric field strength below $40\,kV/m$ to avoid cell damage, especially in the half-decade range above the crossover frequency.

4.2 Cell Characterization

Combined measurements of the DEP crossover frequency and the ROT spectrum were used to derive dielectric parameters of cells according to the procedure described in Section 3.3.5.2. These parameters applied in the corresponding model allow to estimate the DEP response of cells under varying circumstances. Cytoplasmic permittivity and conductivity are taken from literature [PT07] because their influence is negligible. They are fixed to $\sigma_{p2} = 0.7\,S/m$ and $\epsilon_{p2} = 90$ for all curve fitting calculations.

T-Lymphocytes

Electrorotation and crossover frequency experiments were performed at a medium conductivity of 10m S/m and 40 mS/m, respectively. The best fit for *T2-lymphocytes* at $\sigma_m = 10\,mS/m$ according to the single-shell model is illustrated in Fig. 4.3. The calculated membrane capacitance is with $11.7\,mF/m^2$ in a usual range found by others [PT07, YHW+99]. The derived values for *Jurkat* cells are $9.7\,mF/m^2$ and $730.4 S/m^2$ for the membrane capacitance and conductance, respectively (Fig. 4.4). The reduced capacitance and simultaneously increased conductance compared to the first case is attributed to time-dependent ion leakage of the membrane.

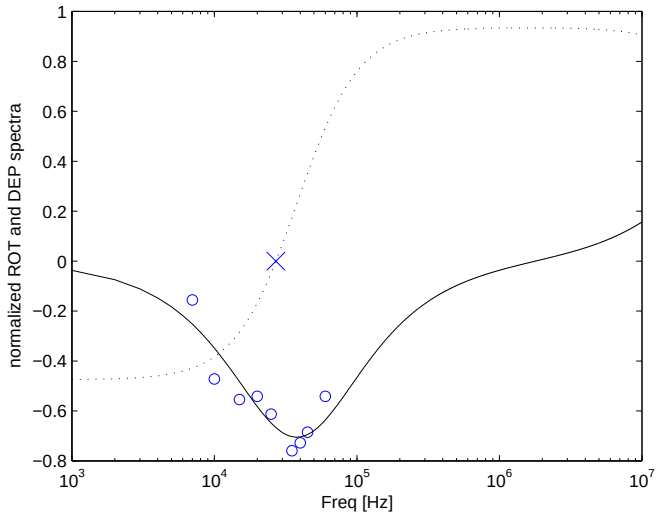

Figure 4.3: Experimental ROT spectrum and crossover frequency of T2-lymphocytes at $\sigma_m = 10\,mS/m$. Lines give the best fit to the thin-shell model. Cell radius: $R = 7\,\mu m$. Values obtained for the membrane capacitance c_m and conductance g_m are $11.7\,mF/m^2$ and $47.62\,S/m^2$, respectively.

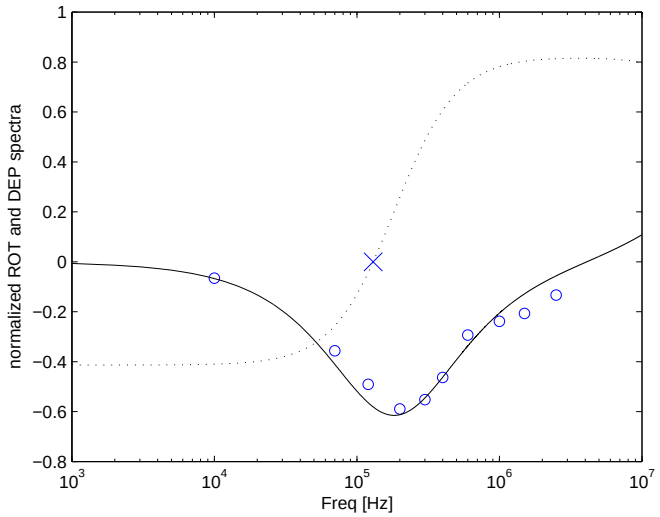

Figure 4.4: ROT spectrum and crossover frequency of *Jurkat* T-lymphocytes at $\sigma_m = 41.5\,mS/m$ and best fit to the thin-shell model. Membrane capacitance c_m is $9.7\,mF/m^2$, membrane conductance $730.4\,S/m^2$

Saccharomyces cerevisiae

The yeast cell envelope consists of a double lipid membrane of about $7\,nm$, a thin periplasmic space of $3.5-4.5\,nm$ and a thick cell wall of $100-200\,nm$ [Fel05]. For the curve-fitting procedure the two-shell model is applied, representing the membrane and the cell wall. The thickness of the wall is assumed to be $150\,nm$ and the values of its permittivity ϵ_{p1} and the membrane conductance

g_m are taken from literature [HHPW92]. The best fit at $40\,mS/m$ and the estimated values of c_m and σ_{p1} are given in Fig. 4.5.

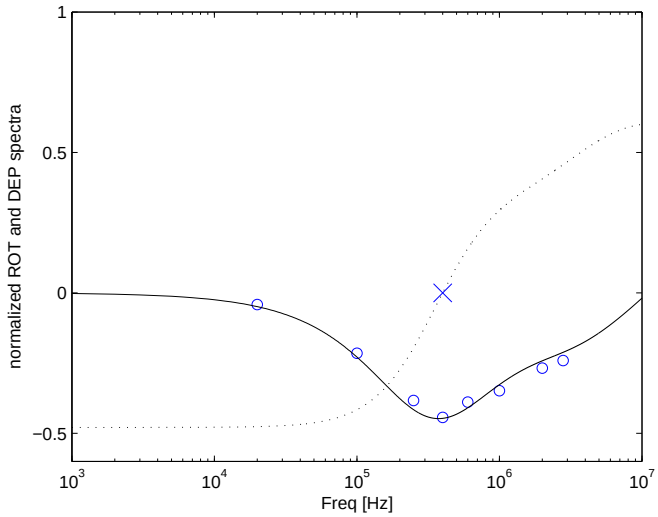

Figure 4.5: ROT spectrum and crossover frequency for yeast at $\sigma_m = 40\,mS/m$. Parameters for the two-shell model: $R = 2.36\,\mu m$, $\delta_w = 150\,nm$, $g_m = 33\,mS/m^2$, $\epsilon_{p1} = 60\epsilon_0$ Estimated Values: $c_m = 10.3\,mF/m^2$, $\sigma_{p1} = 11.6\,mS/m$.

L. Casei

Lactobacillae are gram-positive non-motile bacteria. The cell envelope consists of the cytoplasmic membrane and an outer cell wall, $10 - 50\,nm$ thick. In contrast to gram-negative bacteria there is only a thin periplasmic space between the membrane ant the cell wall. [BB81]
Although Kakutani *et al.* [KSS93] derived a shell model for ellipsoids, the easier to handle spherical model is used in this case because both of them have some unrealistic assumptions. Fig. 4.6 shows the results of the parameter estimation for a two-shell spherical model.

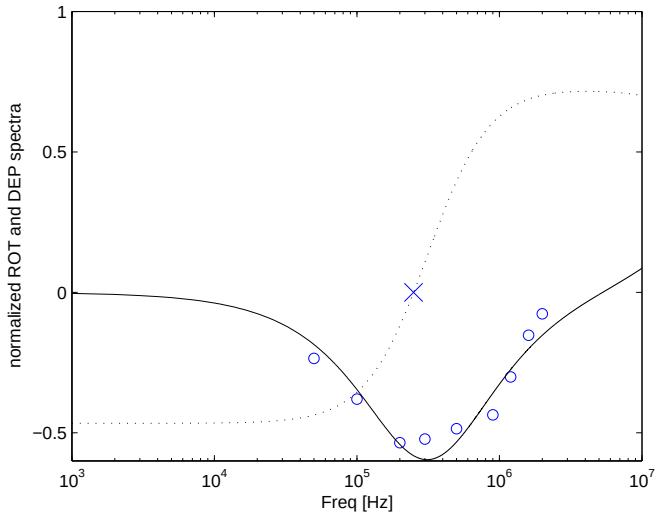

Figure 4.6: *L. casei*: spectra at $\sigma_m = 2.3\,mS/m$. Two-shell best fit for $R = 1.2\,\mu m$, $\delta_w = 20\,nm$, $g_m = 100\,mS/m^2$, $\epsilon_{p1} = 60\epsilon_0$. $c_m = 7.3\,mF/m^2, \sigma_{p1} = 10.2\,mS/m$ derived.

Nannochloropsis sp.

Young cells of this marine alga appear naked. Mature cells exhibit a thin cell wall of 10-30 nm [RZB+03]. For this reason both, the thin-shell and the two-shell model are applied to fit the experimental data. With both models the same value of $c_m = 3.5\,mF/m^2$ was calculated. In the thin-shell case the membrane conductance g_m was estimated to $4020\,S/m^2$. For the the two-shell model the conductivity of the cell wall σ_{p1} was $0.22\,S/m$. The additional parameters needed in the two-shell model are: $\delta_w = 20\,nm, g_m = 100\,mS/m^2, \epsilon_{p1} = 60$.

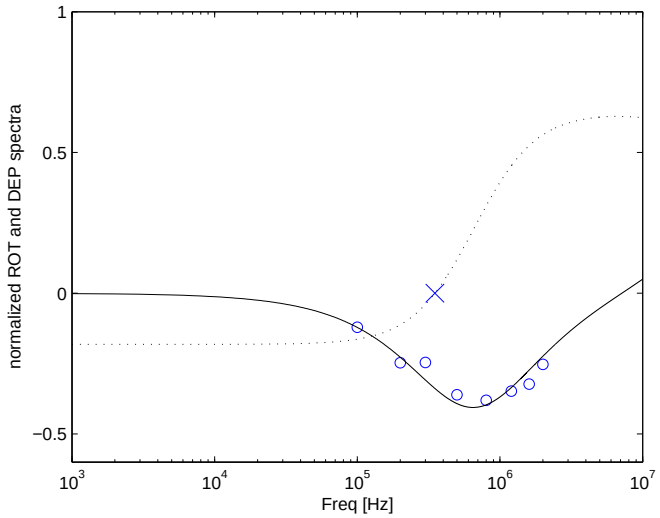

Figure 4.7: *Nannochloropsis sp.* thin-shell best fit for $\sigma_m = 10\,mS/m$, $R = 1.35\,\mu m$. $c_m = 3.5\,mF/m^2, g_m = 4020\,S/m^2$ derived.

Isochrysis galbana

Isochrysis cells have no distinct cell wall like other algae. Therefore, the thin-shell model is applied to predict their dielectric properties. As seen from Fig. 4.8 the thin-shell model fits the data well, but fails to yield realistic values for the membrane capacitance. On the other hand, a two-shell model with common values of membrane capacitance does not fit the experimental data. Since there was no evidence in literature for an abnormal cell structure, the origin of the extraordinary high crossover frequency remains unclear.

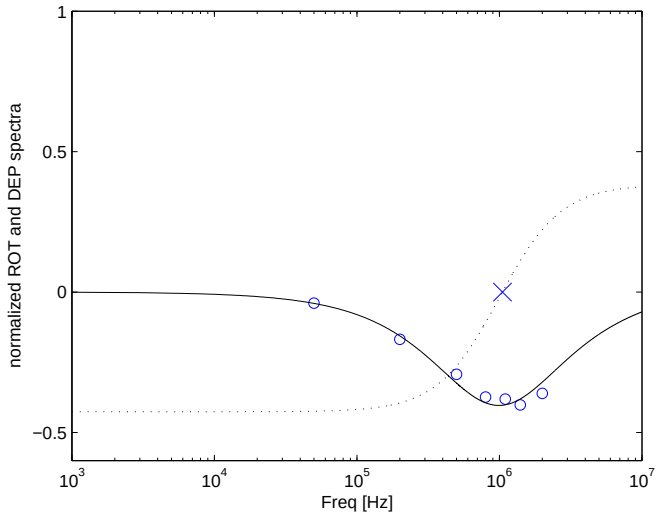

Figure 4.8: *Isochrysis galbana:* ROT spectrum and crossover frequency at $\sigma_m = 10\,mS/m$. Values calculated by the thin-shell model: $c_m = 0.7\,mS/m^2, g_m = 341\,S/m^2$.

Oocystis sp.

For the huge Oocystis aggregates only pDEP behaviour was observed over the entire spectrum. Since there was no crossover frequency, even at a medium conductivity of $60\,mS/m$ and frequencies below $1\,kHz$, it was not possible to obtain dielectric properties from electrorotation studies. Nevertheless, these cells serve as models to investigate cell separation by pDEP forces.

4.3 Separation Results

In order to achieve a continuous separation, a sample with two different cell types is pumped through the microchannel. To separate the cells, two distinct forces perpendicular to the flow are necessary. These forces can be produced either by dielectrophoresis or by sheath flows, focusing the sample stream to a desired position. The fabricated DEP devices were utilized to verify the separation by opposed DEP forces, nDEP only and travelling wave DEP. The results and the separation efficiencies are discussed in the following subsections.

4.3.1 Separation by Opposed DEP Forces

As already stated in Section 2.3 two cell types can be separated in the frequency band between their crossover frequencies. In this band a DEP force with positive sign acts on one cell type and a negative DEP force on the other. This is shown in Fig. 4.9(a) for *Saccharomyces cerevisiae* and *Isochrysis galbana*. The red line indicates the frequency, at which the experiment in Fig. 4.9(b) was conducted. Yeast cells were attracted to the electrodes, while *Isochrysis galbana* (dark brown) collected at the center.

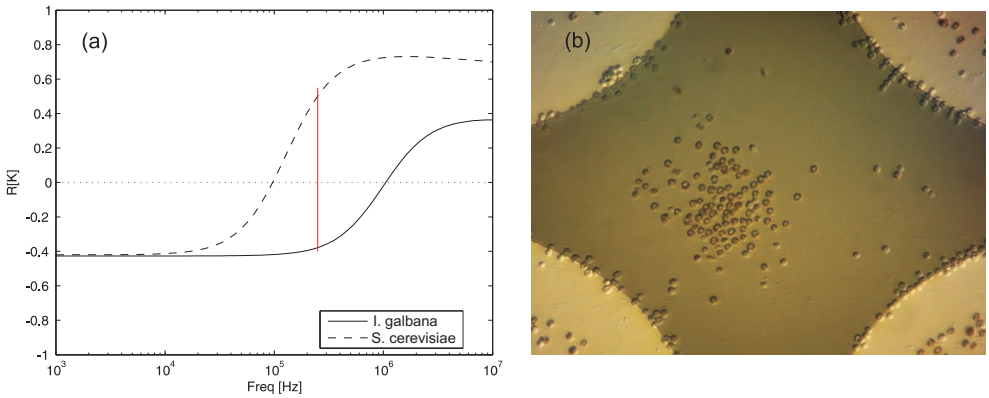

Figure 4.9: Opposed DEP forces for *Saccharomyces cerevisiae* and *Isochrysis galbana*: (a) Simulation of $\mathcal{R}[K]$. (b) Spatial separation with quadupolar electrodes at $\sigma_m = 10\,mS/m$, $250\,kHz$ and $5\,V$.

The advantage of this principle, used in a continuous separation process, is that it works without any focusing of the sample stream. Therefore, only one pump is needed to move the cells along the channel. A major drawback is that cells might get trapped on the electrodes' edges by high pDEP forces and insufficient drag force to move them further. However, in a previous work it was shown that it is possible to move human cells along a strip electrode by positive DEP force. The channel height h_C of that device was, as in the present work, $30\,\mu m$. [DKWV09]
In this work, experiments with T-lymphocytes, yeast and *Oocystis* cells were carried out to prove the use of the designed devices for pDEP application. Fig. 4.10 shows the cell distribution for *Jurkat* cells used with the triangular electrode design. Although the number of cells in the watched time frame was low, distinguishable y-positions for pDEP and nDEP, respectively, were observed. Trapping was not a problem at the settings used in this experiment. As expected from theory, pDEP showed a better efficiency than nDEP at the same supply voltage.

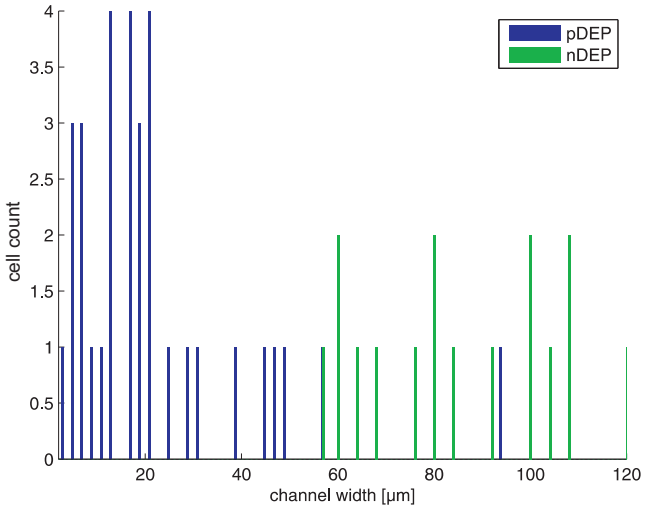

Figure 4.10: Triangular electrodes: Cell distribution for pDEP $(4\,V, 0.1\,\mu l/min, 1\,MHz)$ and nDEP $(4\,V, 0.1\,\mu l/min, 1\,kHz)$.

Trapping of cells depends upon the electrode geometry, the applied voltage, the fluid velocity and the ratio of the cell size to the channel height. The fluid velocity for typical channel dimensions used in DEP experiments is simulated in Fig. 4.11. The grey circles (4.11(b)) indicate cells of the size of yeast and T-lymphocytes. In a pDEP regime cells are attracted to the electrodes at the bottom of the channel. Smaller cells experience a smaller value of the fluid velocity and tend to stick to the electrode edges. In contrast, larger cells are dragged along by the higher fluid velocity. Simply increasing the flow rate does not solve the problem because levitated cells would move too fast to be reliably deflected by the DEP force. It was shown, that for cells with $R \approx h_C/4$ a stable balance between fluid drag and pDEP force is possible. Therefore, the opposed DEP forces serve as a convenient way for cell separation.

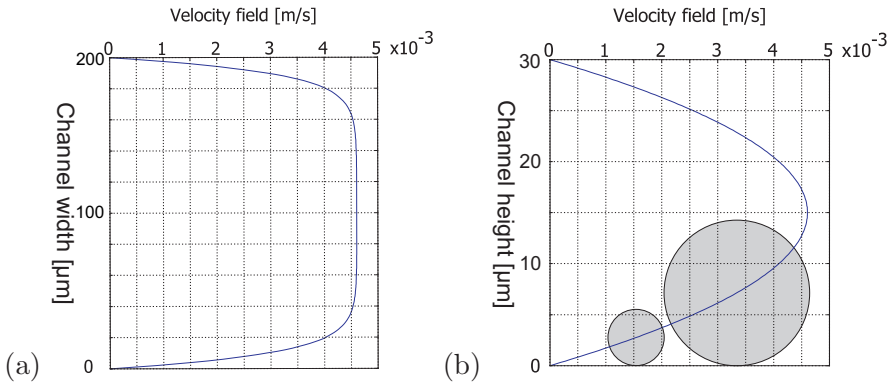

Figure 4.11: Fluid velocity simulations for a channel with $w_C = 200\,\mu m$ and $h_C = 30\,\mu m$ according to Section 3.1.1 (flow rate: $1\,\mu l/min$). (a) Cross-section in y direction at $z = 15\,\mu m$. (a) Cross-section in z direction at $y = 100\,\mu m$. Circles represent cells of $R = 2.8\,\mu m$ and $R = 7\,\mu m$, respectively.

The separation of yeast and *Oocystys sp.* was shown with the interdigitated, castellated and the

interdigitated, elliptical electrodes. At a medium conductivity of $40\,mS/m$ and $100\,kHz$ yeast cells were moved outwards and *Oocystys sp.* were attracted to the center. It turned out that the castellated electrodes show a better performance for pDEP included separation. *Oocystys* cells tended to have a short stay at the elliptical electrodes, whereby following cells were displaced. In contrast, they moved linearly along the edge of the castellated electrodes. The separation result is illustrated in Fig. 4.12. Yeast cells were splitted into two well defined subpopulations at the channel walls. Only a few, perhaps unviable cells remained at the center. For *Oocystys sp.* cells two peaks near the electrodes' edges can be observed. The spreading of the cells is correlated to fluctuations of the fluid velocity.

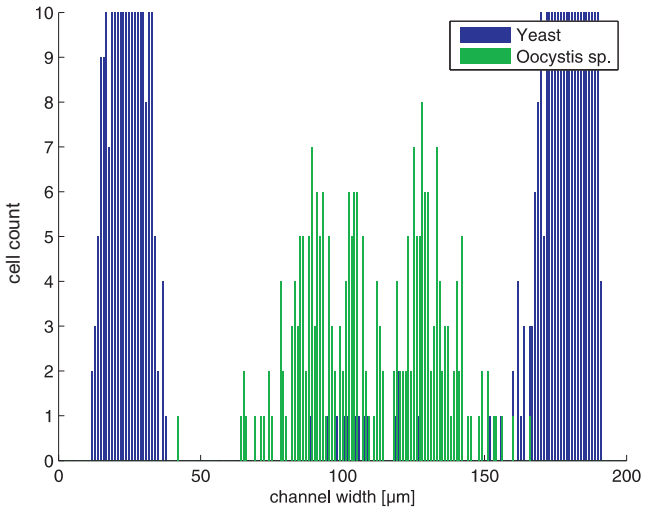

Figure 4.12: Separation result for opposed DEP forces. Interdigitated, castellated electrodes at $3.5\,V$, $40\,mS/m$, $100\,kHz$ and $0.15\,\mu l/min$).

Besides the assumption of a certain cell size to utilize pDEP, the nDEP force for the other cell type should be in a comparable range. A higher voltage, needed to increase the nDEP force on smaller cells, gives rise to cell trapping or cell damage. Therefore, the separation by opposed DEP forces is assumed to be most effective for cells of similar size.

4.3.2 nDEP-based Separation

As already illustrated in Section 3.1.2.4, the separation efficiency of this principle depends upon the focusing of the cell sample, the difference of $\mathcal{R}(\underline{K})$ of the included cells and their size. Experiments were performed using the triangular and the interdigitated, castellated electrodes. In the first device the sample stream is directed to the high electric field side. For the castellated electrodes two side ports are necessary to direct the sample towards the central region. Since the latter was more sensitive to flow rate fluctuations, a more stable and robust separation was achieved with the triangular electrodes.
In order to prove the separation efficiency, a mixture of yeast and *Nannochloropsis sp.* was used. The size distribution of both cell types was determined by a *Beckman* coulter counter (Fig. 4.13(a)). The overlap induces low separation efficiency for only rough focusing, as used in the experiments. Fortunately the real part of the Clausius-Mosotti factor is more negative for

yeast than for *Nannochloropsis sp.* at a medium conductivity of 10 mS/m (Fig. 4.13(b)). This enhances the separation efficiency.

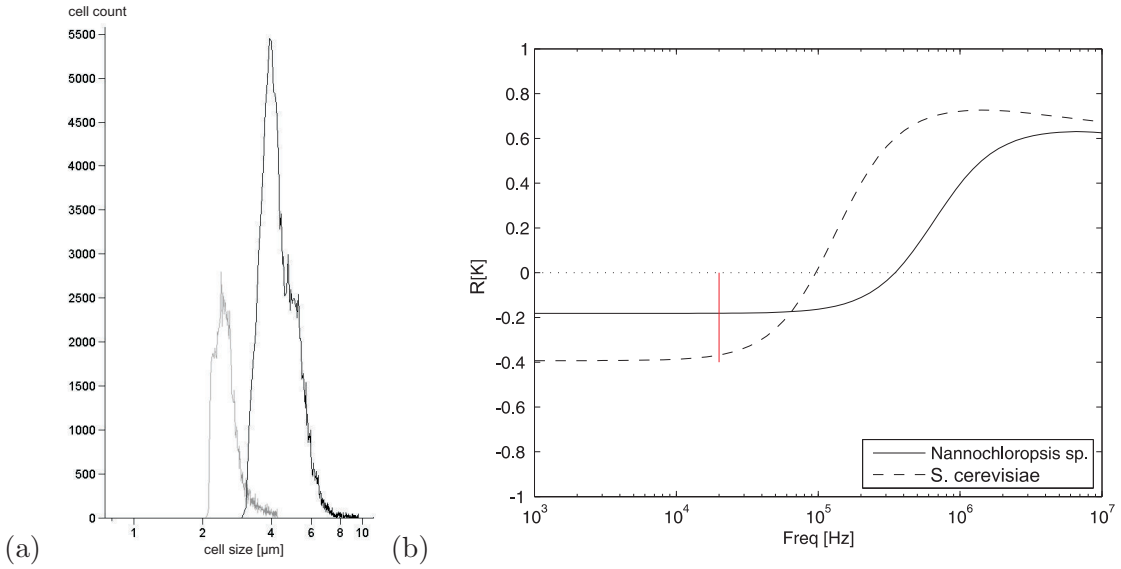

Figure 4.13: (a) Cell size distribution for *Nannochloropsis sp.* (grey) and Yeast (black). (b) Simulated DEP response at 10 mS/m.

The result is given by Fig. 4.14. Without an applied voltage, the cells left the channel in a distribution determined by the ratio of the sample and the sheath flow. Applying the voltage yielded a distribution shown by the green bars. While *Nannochloropsis* cells were distributed within a short range, the yeast cells left the device on the right side. An overlap appeared in a short area between 65 and 75 μm only. A drawback of the triangular electrodes is the high voltage, needed to move these small cells reliably.

Another possibility for nDEP based separation would be to operate the device at the lower crossover frequency of the included cells, or even slightly above. In this case only the cells with the higher crossover frequency experience a negative DEP force. This strategy is adequate for cell types of similar size. It does not work e.g. to separate bacteria from human cells. The electric field strength necessary to move bacteria, would burst the other cells.

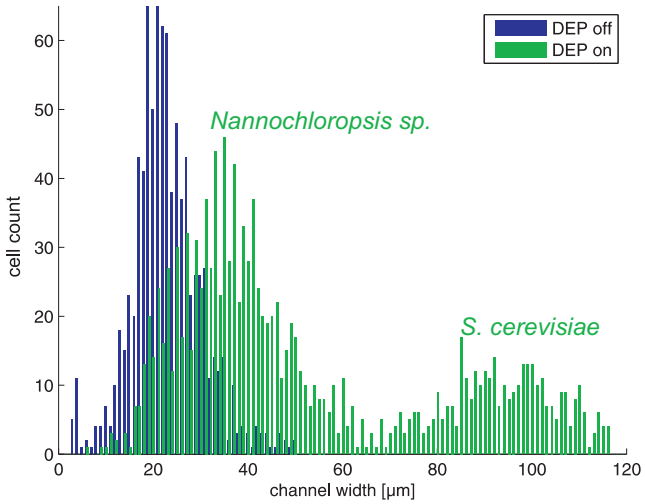

Figure 4.14: Separation result for a mixture of *S. cerevisiae* and *Nannochloropsis*. Triangular electrodes were used at $10m\,S/m$, $20\,kHz$ and $10\,V$. Flow rates: $0.05\,\mu l/min$ sample flow, $0.15\,\mu l/min$ sheath flow. Two distinct populations of *S. cerevisiae* and *Nannochloropsis* with only a small overlap can be observed when DEP is on.

4.3.3 Separation by twDEP

Travelling electric fields exert a force on cells proportional to the imaginary part of the Clausius-Mosotti factor. Remarkably, the commonly used spiral electrodes did not work as expected. The twDEP force was observable at the first turns of the spiral, but vanished towards the center. The reason is a potential drop due to the resistance of the long electrodes.
In contrast, good separation results were achievable with the parallel electrode configuration. The idea of the separation is shown in Fig. 4.15. The sample is inserted through one inlet and pushed towards the sidewall by a sheath flow from the second (Fig. 4.15(a)). The target cells, chosen by an appropriate frequency, are forced to the other side of the channel. The trajectories of two cells influenced by the travelling field, are depicted in Fig. 4.15(b). Since this force showed to be very selective, an efficient separation is possible. The target cells leave the channel on the upper side, while the rest are almost unaffected Fig. (4.15(c)).

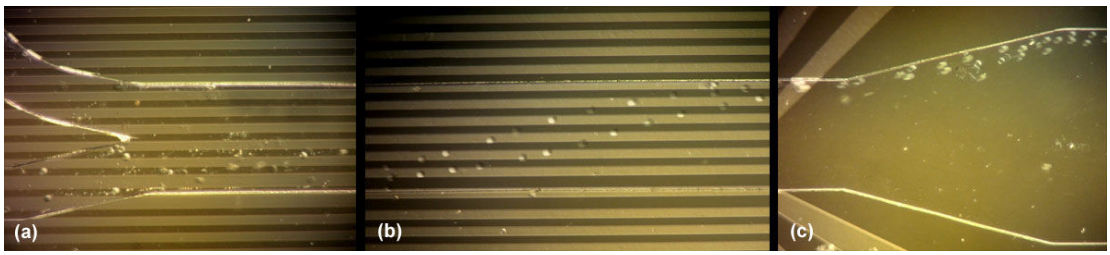

Figure 4.15: Separation by travelling electric field. (a) Cells enter the device on one side of the channel. (b) Target cells are moved to the other side and (c) leave the channel separated from the others.

With this method, separation of yeast and *L. casei*, viable and unviable yeast, T-lymphocytes from debris (dead cells and *L. casei*) and yeast from *Nannochloropsis sp.* was shown. The

most interesting cases of separation, cells from bacteria and yeast from *Nannochloropsis sp.* are discussed in detail. The first is important because of its potential application in cell culture purification and bacterial contamination detection. For the latter it is interesting to compare the separation efficiency to nDEP based separation. Comparing the negative ROT peaks of Fig. 4.16 reveals regions where the values of $\mathcal{I}[\underline{\mathcal{K}}]$ differ strongly. This difference in combination with the different cell size suggests an efficient way of separation. It is straightforward to verify that the force difference for T-lymphocytes and *L. casei* is enormous.

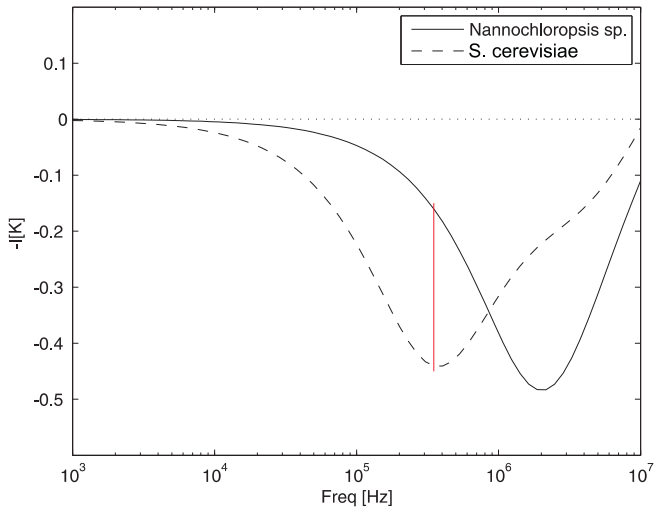

Figure 4.16: Simulation of the negative ROT peak of yeast and *Nannochloropsis sp* . The red line refers to the frequency in the separation.

The result of twDEP experiments with *Jurkat* T-lymphocytes and *L. Casei* is illustrated in the histogram 4.17. Only T-lymphocytes are considered in the histogram, because *L. Casei* are too small for an automated detection. It can be seen that without an applied voltage 100 % of the counted T-lymphocytes left the device on the right side of the channel. When a voltage was applied, viable cell could be found close to the other channel wall. Altogether, 86.5 % of the T-lymphocytes were counted on the left side. The remaining 13.5 % of unaffected cells seemed to be unviable. Also not affected were *L. casei* bacteria and debris, leaving the device as without a voltage supply.

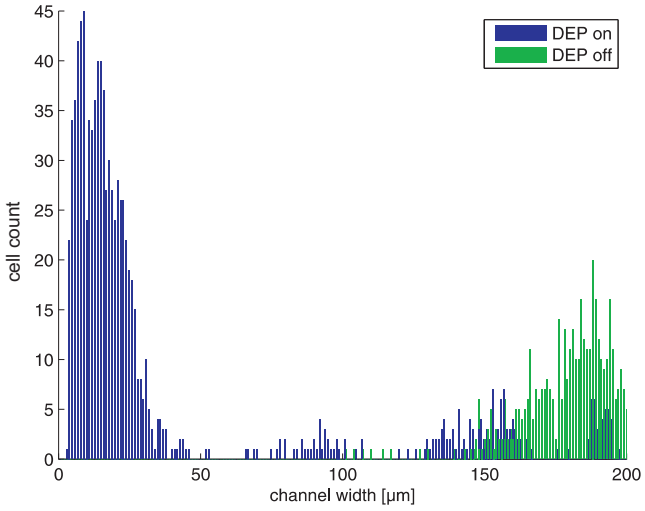

Figure 4.17: Separation of *Jurkat* T-lymphocytes from debris at $40\,mS/m$, $100\,kHz$, $3.5\,V$, $0.1\,\mu l/min$ sample flow and $0.15\,\mu l/min$ sheath flow.

A similar result is shown in Fig. 4.18 for the separation of yeast and *L. casei*. In this case the cell mixture was focused to the left side of the channel. Yeast cells were selectively moved to the right side when the voltage was applied. *L. casei* are not considered in the cell count due to their small size, but left the device in the region of the blue bars.
These results show that twDEP is well suited for purification of cells from a certain culture. However, to reliably detect bacteria in a contaminated culture, a second stage is neccesary to remove bacteria from debris and focus them to a distinct position.

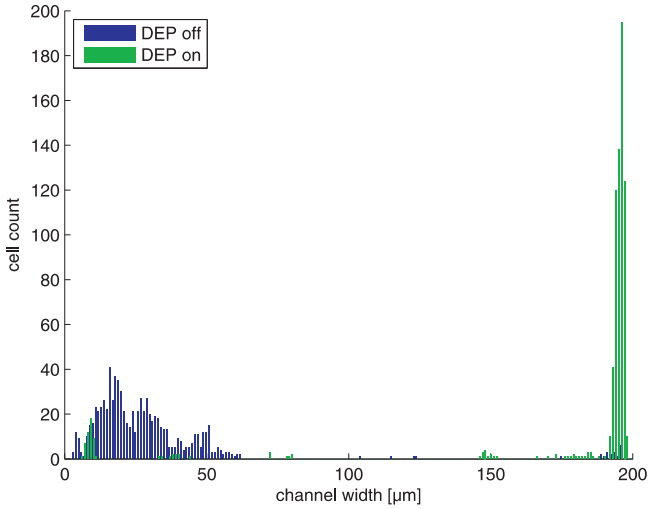

Figure 4.18: Separation of yeast from *L. casei* at $40\,mS/m$, $350\,kHz$, $5\,V$, $0.1\,\mu l/min$ sample flow and $0.15\,\mu l/min$ sheath flow.

In Fig. 4.19 the separation result for yeast and *Nannochloropsis sp.* is illustrated. *Nannochloropsis* cells show a relative broad distribution, depending on the focusing and twDEP induced movement

to the left. For yeast cells a clear peak near the left channel wall is observable. Since these cells are lifted by a nDEP force, they move in a channel height, where the fluid velocity is much slower (Fig. 4.11(b)). For this reason the cell count for yeast is much less than for *Nannochloropsis sp.* Remarkably, there is another peak of yeast cells, near the right channel wall. These cells are lifted above the first electrode of the array by nDEP and do not experience the travelling field. This problem can be addressed by aligning the channel not parallel to the electrodes and by reducing the electrodes width for small cells.

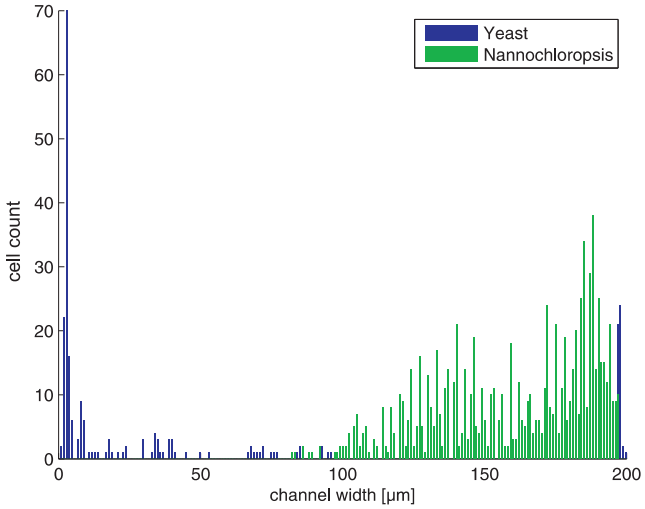

Figure 4.19: Separation of yeast and *Nannochloropsis sp.* at $40\,mS/m$, $350\,kHz$, $5\,V$, $0.1\,\mu l/min$ sample flow, $0.15\,\mu l/min$ sheath flow.

Besides the separation of cell mixtures, twDEP has the capability for accurate positioning of cells within a DEP device. In Fig. 4.20(a) *Nannochloropsis sp.* are moved to distinct positions by disrupting the travelling wave after every forth electrode. Fig. 4.20(b) shows the accumulation of cells in a high concentration at the center. These experiments suggest twDEP as a convenient way for handling of on-chip cell cultures. By changing the excitation sequence of the electrodes and the frequency it is even possible to handle different cell types in one device independently.

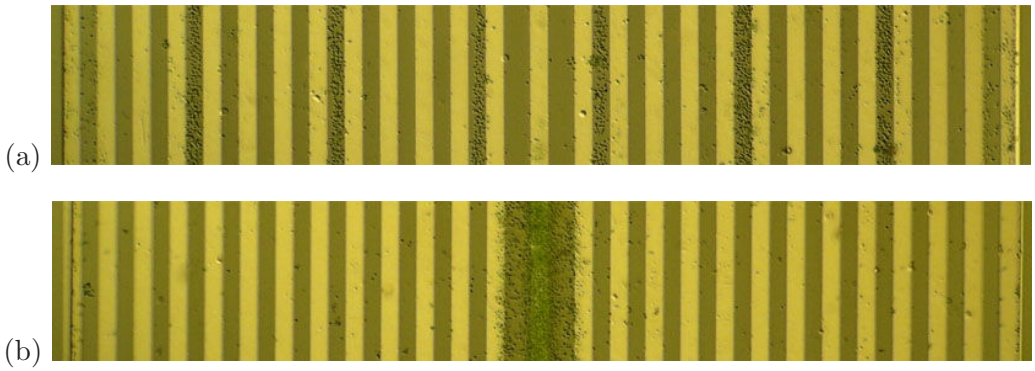

Figure 4.20: Cell positioning by travelling electric fields. (a) *Nannochloropsis* cells are collected at distinct positions. (b) Accumulation at the center.

5 Conclusion

Microfluidic devices with different electrode structures for the separation of cell cultures have been presented. The well known electrorotation technique has been used to estimate dielectric parameters of different cell types. Although the derived values for cells such as T-lymphocytes and *Saccharomyces cerevisiae* (baker's yeast) showed good agreement to literature data, unrealistic values for *Isochrysis galbana* were obtained.
Separation of cell mixtures has been shown by opposed DEP forces, nDEP and twDEP. The separation by opposed DEP forces has the advantage over the others, that no pre-focusing of the sample is necessary. On the other hand its application is limited to cases of similar cell size and a minimum cell size to channel height ratio.
Cell separation by pure nDEP forces is a favoured approach. However, good results are only achievable when the cells have distinct sizes. An adequate sample focusing is crucial for the separation efficiency.
Travelling wave DEP showed to be the most flexible method. Highly efficient separation of a variety of cell mixtures was achievable with only rough sample focusing. Smart signal superposition, as shown by Pethig *et al.* [PTS03] could make hydrodynamic focusing unnecessary.

5.1 Outlook

This section provides suggestions and improvements for future cell characterization and separation measurements and a next generation of DEP devices.

5.1.1 Cell Characterization Improvements

To use the entire spectrum for electrorotation measurements, a voltage supply with a higher frequency range is necessary. Since the co-field rotation peak usually is located in the 100 MHz range, it has not been possible to estimate dielectric parameters of the cytoplasm. Furthermore, the accuracy of membrane parameter estimation increases slightly with a higher frequency limit [GBW95]. Although ROT and DEP measurements have been performed with the same sample in one device, more points of the DEP response could be measured to ensure consistence of the ROT and DEP data. Argand plots of $\mathcal{I}[\underline{K}]$ vs. $\mathcal{R}[\underline{K}]$ show a half-circle for each relaxation process when the data is consistent. The Argand plot for T-lymphocytes according to the thin-shell model is depicted in Fig. 5.1. For the two-shell model a third half-circle is added but superposed to the

others. Additional electrodes on the device could be useful to check the temperature and the medium conductivity during measurements.

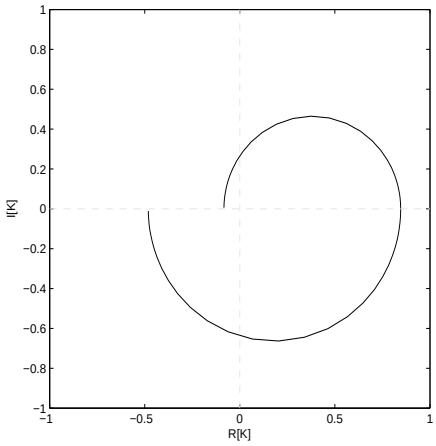

Figure 5.1: Simulated Argand plot for T-lymphocytes

5.1.2 Separation Measurement Improvements

For microfluidic devices it is important that the outlets are identical to ensure a proper division of the liquid. In the present setup the tubes of the holder affect the flow in the device. Output bins directly on the chip could solve this problem. Furthermore, hydrodynamic focusing complicates the setup and causes back flow of cells into the sheath inlets when connecting the device to the holder. Combining the advantages of the presented devices in multi-stage systems would enable highly efficient separation without the need of pre-focusing. The schematic Fig. 5.2 shows a possible two-stage device. The elliptical electrodes, which produce a well defined nDEP force at a low voltage, force the cells towards the channel walls. In the second stage, one cell type is moved back to the center of the device by twDEP as illustrated in Section 4.3.3.

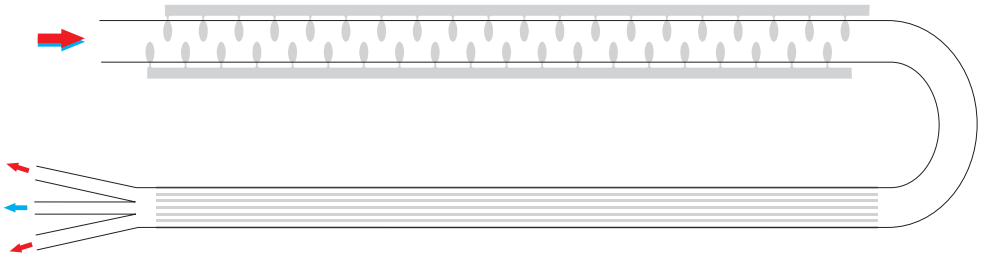

Figure 5.2: Schematic of a two-stage cell fractionation system

Appendix

A Two-shell Model Parameter Sensitivity

The two-shell model shows a similar sensitivity towards ϵ_{p3}, σ_{p3}, c_m and g_m as already shown for the thin-shell model in Fig. 2.5. The sensitivity to the cell wall properties is illustrated in Fig. A1. Additionally the spectra in case of cell radius variation are shown in Fig. A1(d). It can be seen that the impact of the radius is comparable to that of c_m. Thus, an overestimated radius results in a reduced value of c_m, and vice versa.

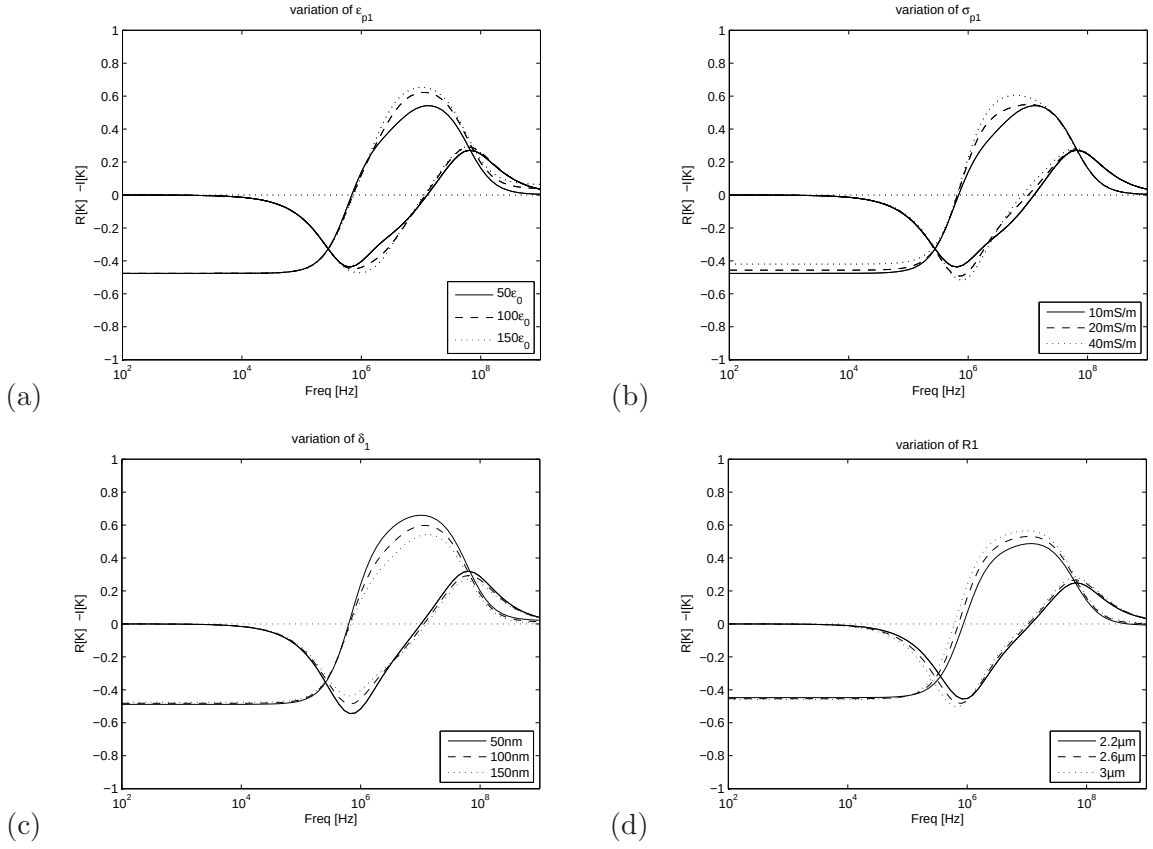

Figure A1: Two-shell model parameter sensitivity ($\sigma_m = 40\,mS/m$): (a) Cell wall permittivity ϵ_{p1}. (b) Cell wall conductivity σ_{p1}. (c) Cell wall thickness δ_1. (c) Cell radius $R1$.

B Device Masks

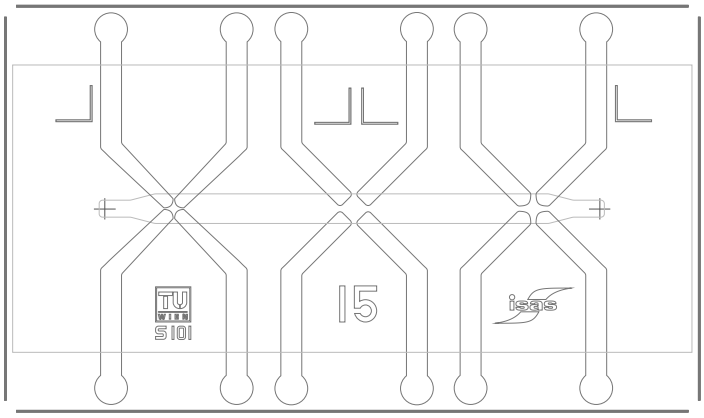

Figure B1: Quadrupolar electrodes.

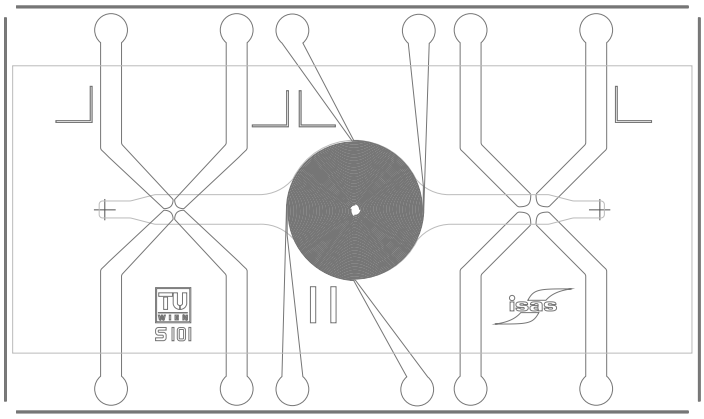

Figure B2: Quadrupolar and spiral electrodes.

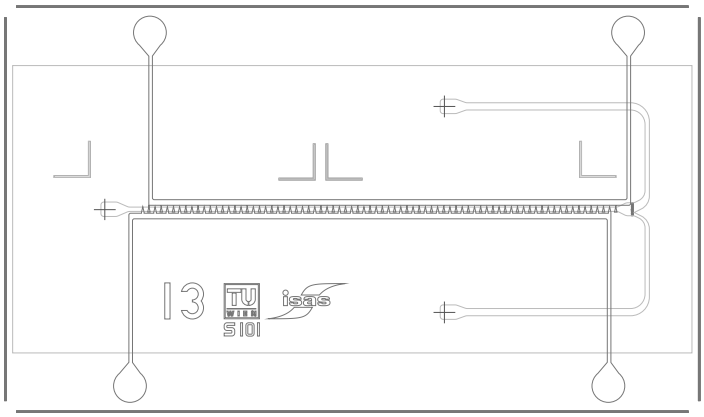

Figure B3: Triangular electrodes.

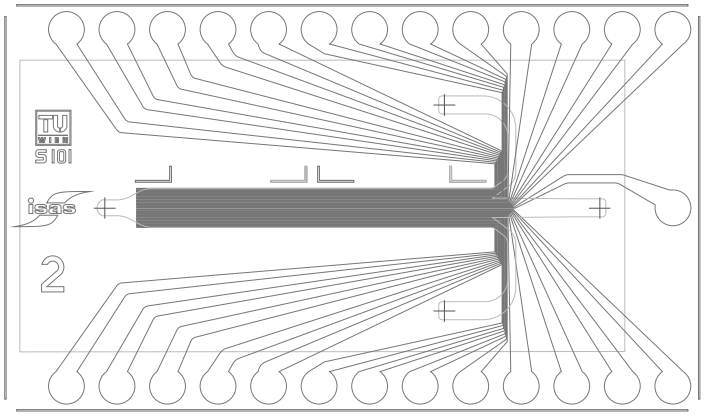

Figure B4: Parallel travelling wave electrodes.

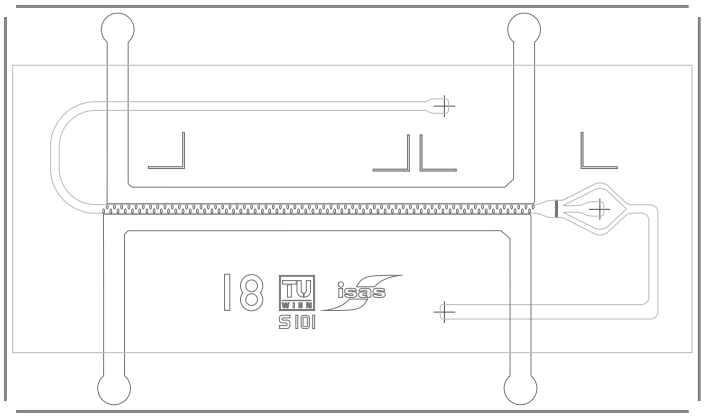

Figure B5: Interdigitated, elliptical electrodes.

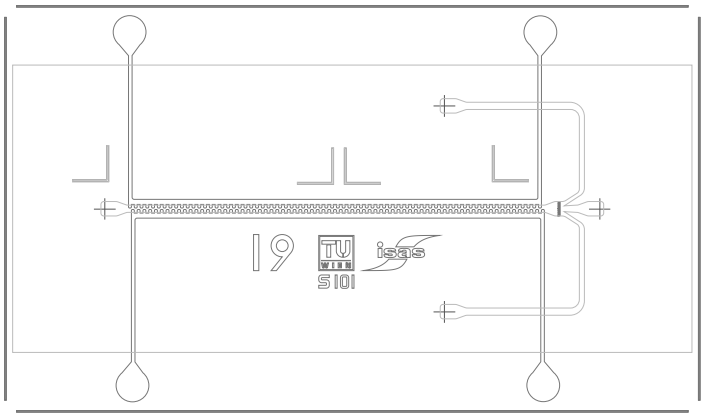

Figure B6: Interdigitated, castellated electrodes.

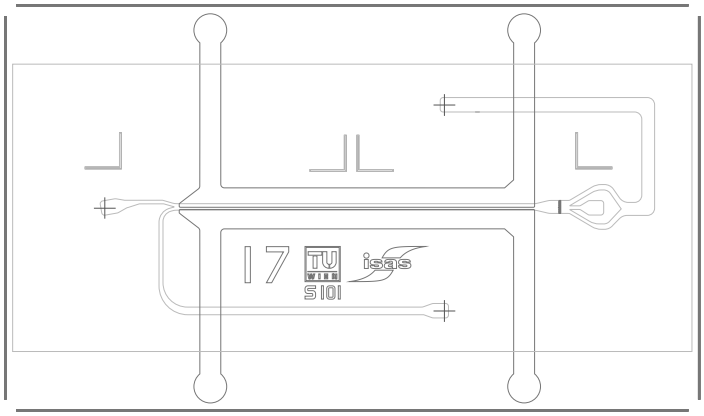

Figure B7: Parallel strip electrodes.

C Trajectory Simulation

trajectory.m

```
clear;
clc;
close all;

eps_m=78;
eps_0=8.854e-12;

%Medium viscosity
eta=1.37e-3;

%Time step
dT=8e-3;

%Fluid velocity
vscale=0.2;

%Number of DEP actuators-2
reps=68;

%Load FEM data, simulated with COMSOL Multiphysics
fem_flow       = flload('flownarrow.mph');
fem_fdep       = flload('fdepnarrow.mph');

%Start points of cells
sp=[
    0e-6 40e-6 5e-6;...
    0e-6 60e-6 5e-6;...
    0e-6 80e-6 5e-6;...
    0e-6 100e-6 25e-6;...
    0e-6 120e-6 25e-6;...
    ]

points=size(sp,1);

%///////////////PDEP ////////////////////////////////////
```

```
K_cell=0.3;
%Radius of T Lymphocytes
R=6e-6;
%DEP scale factor U^2*2*pi*R^3*eps_m*eps_0
Fscale=4*2*pi*R^3*eps_m*eps_0;

for yp=1:1:points
clear pos;
pos(1,:) = sp(yp,:);
i=1;

%1st two elements
while (pos(i,1)<280e-6) %end position of trajectory calculation

    %Call getVelocity.m to get fluid velocity in pos
    v_liq = vscale*[getVelocity(fem_flow,pos(i,:)) 0 0];

    %Call getVelocity.m to get DEP force in pos
    F_dep =Fscale*K_cell* getFdep(fem_fdep,pos(i,:));

    %Calculate new cell velocity
    v_p   = F_dep/(6*pi*eta*R)+v_liq;
    %Calculate next position
    pos(i+1,:) = pos(i,:)+v_p.*ΔT;

    %Channel wall boundaries
             if pos(i+1,3)<R pos(i+1,3)=R; end;
             if pos(i+1,3)>30e-6-R pos(i+1,3)=30e-6-R; end;
             if pos(i+1,2)<20e-6+R pos(i+1,2)=20e-6+R; end;
             if pos(i+1,2)>220e-6-R pos(i+1,2)=220e-6-R; end;

             disp(sprintf('Position: %i %i %i um',round(pos(i,:).*1e6)));
             i=i+1;
end;

i=i-1;

%pos1: relative position in the repeated channel part
pos1=[pos(i,1) pos(i,2) pos(i,3)]

%Repeat DEP elements
for n=1:1:reps
    %Repeated channel part is shorter
    pos1=[pos1(1)-160e-6 pos(i,2) pos(i,3)]

while (pos1<280e-6)

    v_liq = vscale*[getVelocity(fem_flow,pos1) 0 0];
    F_dep = Fscale*K_cell*getFdep(fem_fdep,pos1);
    v_p   = F_dep/(6*pi*eta*R)+v_liq;

    %Absolute position in channel
    pos(i+1,:) = pos(i,:)+v_p.*ΔT;
    pos1 = pos1+v_p.*ΔT;
    if pos1(3)<R pos1(3)=R; end;
    if pos1(3)>30e-6-R pos1(3)=30e-6-R; end;
    if pos1(2)<20e-6+R pos1(2)=20e-6+R; end;
    if pos1(2)>220e-6-R pos1(2)=220e-6-R; end;
```

```
    if pos(i+1,3)<R pos(i+1,3)=R; end;
    if pos(i+1,3)>30e-6-R pos(i+1,3)=30e-6-R; end;
    if pos(i+1,2)<20e-6+R pos(i+1,2)=20e-6+R; end;
    if pos(i+1,2)>220e-6-R pos(i+1,2)=220e-6-R; end;

    disp(sprintf('Position: %i %i %i um',round(pos(i,:).*1e6)));
    i=i+1;
end;
i=i-1;
end
figure(1)
hold on
axis([0 max(pos(:,1)) 20e-6 220e-6]);
         xlabel('Channel Length x');
         ylabel('Particle Position y');
plot(pos(:,1)-50e-6,pos(:,2),'r')
plot(linspace(0,max(pos(:,1))),100e-6,'k')
plot(linspace(0,max(pos(:,1))),140e-6,'k')
figure(2)
hold on
axis([0 max(pos(:,1)) 0 50e-6]);
         xlabel('Channel Length x');
         ylabel('Particle Position z');
plot(pos(:,1)-50e-6,pos(:,3),'r')

end
```

getFdep.m

```
function dE = getFdep(fem,pos)
%Gets the DEP force at the actual position from FEM data.

%Check on undefined values
if (pos(1)<0e-6 | pos(2)<0 | pos (3)<0 | pos(2)>120e-6 | pos(3)>30e-6);
    dE='error';
    return;



else
fx=postinterp(fem,'dE_X',pos');
fy=postinterp(fem,'dE_Y',pos');
fz=postinterp(fem,'dE_Z',pos');

dE=[fx fy fz];
end;
```

getVelocity.m

```
function u = getVelocity(fem,pos)
%Gets the fluid velocity at the actual position from FEM data.



%Check on undefined values
if (pos(1)<0e-6 | pos(2)<0 | pos (3)<0 | pos(2)>120e-6 | pos(3)>30e-6);
```

```
    u='error';
    return;

else
u=postinterp(fem,'u',pos');

end;
```

D Curve Fitting Procedure

cmplot.m

```
clc; clear all;close all;
%Experimental ROT values
values =[0.0420 0.2277 0.3137 0.3768 0.3531 0.2964 0.1875 0.1524 0.1325 0.0854]
f=[10e3 70e3 120e3 200e3 300e3 400e3 600e3 1e6 1.5e6 2.5e6]
%Experimental crossover frequency
fc0=130e3;

e0=8.854e-12;
omega=2*pi*f;
oc0=2*pi*fc0;



%Start values
k=0.5;
c_m=18e-3;
g_m=1000;

%Call of fitmodel.m, fitted parameters: c_m, g_m and scaling factor k
[c_m,g_m,k]=fitmodel(omega, values,oc0, c_m,g_m,k)


%Plot experimental ROT values
semilogx(f,-values./k,'bo')
hold on;

fc=1e3:1e3:1e7;
%Call singleshell.m to calculate I[K] with derived values
icmf=imag(singleshell(2*pi*fc, c_m,g_m,k));
%Call singleshell.m to calculate R[K] with derived values
rcmf=real(singleshell(2*pi*fc, c_m,g_m,k));
semilogx(fc,-icmf./k,'-k');
semilogx(fc,rcmf./k,':k');
semilogx(fc0,0,':b','Marker','x','Markersize',15);
xlabel('Freq [Hz]');
ylabel('normalized ROT and DEP spectra');
```

fitmodel.m

```
function [c_m,g_m,k] = fitmodel(omega, values,oc0, c_m,g_m,k)

%Weight factors
V=1;
```

```
W=1;

    %Start values
    sp(1) = c_m;
    sp(2)=g_m;
    sp(3)=k;

%Residual error function; singleshell.m is called with parameters,
%which are unknown at this time @(...)
 model = @(p, omega, values, oc0) (V*sum ...
        (imag(singleshell(omega,p(1),p(2),p(3)))-values).^2 ...
       + W* (real(singleshell(oc0, p(1),p(2),p(3))))^2 );


 options = optimset('TolFun',1e-6,'TolX',1e-6,'MaxFunEval',5000,'MaxIter',5000);
%Apply the Nelder-Mead complex to the model
 estimates = fminsearch(model,sp,options, omega, values, oc0);


    %Return values
    c_m= estimates(1);
    g_m= estimates(2);
    k= estimates(3);
end
```

singleshell.m

```
function cmf= singleshell(omega, c_m, g_m,k)


eps_0 = 8.854e-12;
%Values from literature
eps_c = 60*eps_0;
sig_c = 0.7;
eps_1 = 78*eps_0;
%Medium conductivity at experiments
sig_1 = 41.5e-3;
%Measured cell radius
R    = 7e-6;

    %Complex medium permittivity
     eps_compl_1 = eps_1+sig_1./(i*omega);
    %Effective complex cell permittivity according to the thin-shell model
     eps_compl_2= (c_m-i*g_m./omega)*R.*(eps_c-i*sig_c./omega)./ ...
                  ((c_m-i*g_m./omega)*R+eps_c-i*sig_c./omega);

    %Clausius-Mosotti factor
     cmf=k*((eps_compl_2-eps_compl_1)./(eps_compl_2+2*eps_compl_1));
```

Literature

[Avi07] Avian, J.: *On-chip particle separator basedon dielectrophoresis*, TU Wien, Master thesis, 2007

[AYT90] Asami, K. ; Y., Takahashi ; Takashima, S.: Frequency domain analysis of membrane capacitance of cultured cells (HeLa and myeloma) using the micropipette technique. In: *Biophys. J.* 58 (1990), pp. 143–148

[Baz08] Bazant, M. Z.: AC Electro-osmotic flow. In: Li, Dongqing (Hrsg.): *Encyclopedia of Microfluidics and Nanofluidics*. Berlin, Heidelberg, New York : Springer, 2008, Chapter I, pp. 8–14

[BB79] Bahaj, A.S. ; Bailey, A.G.: Dielectrophoresis of microscopic particles. In: *J. Phys. D: Appl. Phys.* 12 (1979)

[BB81] Bican, P. ; Blanc, B.: Partial Characterization of Lactobacillus lactis Cell Envelope Proteins. In: *Journal of Dairy Science* 64 (1981)

[Bru08] Bruus, H.: *Theoretical Microfluidics*. New York : Oxford University Press, 2008

[CCH+09] Chunag, C.-H ; Chen, Y.-C. ; Hsu, Y.-M. ; Huang, H.-S. ; Hsiao, F.-B. ; Wang, C.-H.: A DEP Chip with Arc-Shape Microelectrode Arrays for the Separation of Different-size Particles. In: *Proceedings of the 2009 4th IEEE International Conference on Nano/Micro Engineered and Molecular Systems*, 2009

[CCHC07] Cheng, I.F. ; Chang, H.C. ; Hou, D. ; Chang, Hs.: An integrated dielectrophoretic chip for continuous bioparticle filtering, focusing, sorting, trapping and detecting. In: *Biomicrofluidics* 1 (2007)

[CGBP97] Chan, K. L. ; Gascoyne, P. ; Becker, F. ; Pethig, R.: Electrorotation of liposomes: verification of the dielectric multi-shell model for cells. In: *Biochimica et Biophysica Acta* 1349 (1997), pp. 182–196

[CP05] Choi, S. ; Park, J.-K.: Microfluidic system for dielectrophoretic separation based on a trapezoidal electrode array. In: *Lab on a Chip* 5 (2005), pp. 1161–1167

[CRG+03] Castellanos, A. ; Ramos, A. ; Gonzalez, A. ; Green, N.G. ; Morgan, H.: Electrohydrodynamics and dielectrophoresis in microsystems: scaling laws. In: *J. Phys. D: Appl. Phys* 36 (2003), pp. 2584–2597

[DKWV09] Driesche, S. v. ; Kostner, S. ; Witarski, W. ; Vellekoop, M. J.: A Strip electrode design for robust continuous cell separation based on positive and negative dielectrophoresis. In: *MicroTAS*, 2009

[Fel05] Feldmann, H.: *Yeast Molecular Biology*. Available online, visited 05.10.2009. 2005. – http://biochemie.web.med.uni-muenchen.de/Yeast_Biol

[FHM91] Fuhr, G. ; Hagedorn, R. ; Müller, T.: Linear Motion of Dielectric Particles and Living Cells in Microfabricated Structures Induced by Traveling Electric Fields. In: *Proceedings. 'An Investigation of Micro Structures, Sensors, Actuators, Machines and Robots'. IEEE* (1991), pp. 259–264

[GBW95] Gascoyne, P. ; Becker, F.F. ; Wang, X.-B.: Numerical analysis of the influence of experimental conditions on the accuracy of dielectric parameters derived from electrorotation measurements. In: *Bioelectrochemistry and Bioenergetics* 36 (1995), pp. 115–125

[GMM+02] Gascoyne, P. ; Mahidol, C. ; M., Ruchirawat ; Satayavivad, J. ; Watcharasitb, P. ; Becker, F.F.: Microsample preparation by dielectrophoresis: isolation of malaria. In: *Lab on a Chip* 2 (2002), pp. 70–75

[GRM00] Green, N.G. ; Ramos, A. ; Morgan, H.: AC electrokinetics: a survey of submicrometre particle dynamics. In: *J. Phys. D: Appl. Phys* 33 (2000), pp. 632–641

[GWHB97] Gascoyne, P. ; Wang, X.-B. ; Huang, Y. ; Becker, F.F.: Dielectrophoretic Separation of Cancer Cells from Blood. In: *IEEE Transactions of Industry Applications* 33 (1997), Nr. 3, pp. 670–678

[HHPW92] Huang, Y. ; Hölzel, R. ; Pethig, R. ; Wang, X.: Differences in the AC electrodynamics of viable and non-viable yeast cells determined through combined dielectrophoresis and electrorotation studies. In: *Phys. Med. Biol.* 37 (1992), Nr. 7, pp. 1499–1517

[HP91] Huang, Y. ; Pethig, R.: Electrode design for negative dielectrophoresis. In: *Meas. Sci. Technol.* 2 (1991), pp. 1142–1146

[HWTP93] Huang, Y. ; Wang, X-B. ; Tame, J.A. ; Pethig, R.: Electrokinetic behaviour of colloidal particles in traveling electric fields: studies using yeast cells. In: *J. Phys. D: Appl. Phys.* 26 (1993), pp. 1528–1535

[Jon95] Jones, T. B.: *Electromechanics of Particles*. Cambride : Camridge University Press, 1995

[Jon03] Jones, T. B.: Basic Theory of Dielectrophoresis and Electrorotation. In: *IEEE Eng Med Biol Mag.* 22 (2003), pp. 33–42

[KL09] Kuo, C.-T. ; Liu, C.-H.: A Bubble-Free AC Electrokinetic Micropump Using the Asymmetric Capacitance-Modulated Microelectrode Array for Microfluidic Flow Control. In: *Journal of Microelectromechanical Systems* 18 (2009), Nr. 1

[KSS93] Kakutani, T. ; Shibatani, S. ; Sugai, M.: Electrorotation of non-spherical cells:

theory for ellisoidal cells with an arbitrary number of shells. In: *Bioelectrochemistry and Bioenergetics* 31 (1993), pp. 131–145

[Lid98] Lide, D. R.: *Handbook of Chemistry and Physics*. 87. Boca Raton : CRC Press, 1998

[LW09] Lian, M. ; Wu, J.: *Microfluidic flow reversal at low frequency by AC electrothermal effect*. http://www.springerlink.com/content/27625857m2252nmw/. 2009. – Published online, visited 15.10.09

[LZW+04] Lastochkin, D. ; Zhou, R. ; Wang, P. ; Ben, Y. ; Cheng, H.C.: Electrokinetic micropump and micromixer design based on ac faradaic polarization. In: *Journal of Applied Physics* 96 (2004)

[MHG99] Morgan, H. ; Hghes, M.P. ; Green, N.G.: Separation of Submicron Bioparticles by Dielectrophoresis. In: *Biophysical Journal* 77 (1999), pp. 516–525

[MP05] Menachery, A. ; Pethig, R.: Controlling cell destruction using dielectrophoretic forces. In: *IEEE Proc.- Nanobiotechnol.* 152 (2005), Nr. 4

[MRV07] Mittal, N. ; Rosenthal, A. ; Voldman, J.: nDEP microwells for single-cell patterning in physiological media. In: *Lab on a Chip* 7 (2007), pp. 1146–1153

[MWI87] Masuda, S. ; Washizu, M. ; Iwadare, M.: Seperation of Small Particles Suspended in Liquid by Nonuniform Traveling Field. In: *IEEE Transactions on Industry Applications* 1A-23 (1987), Nr. 3

[MWK88] Masuda, S. ; Washizu, M. ; Kawabata, I.: Movement of Blood Cells in Liquid by Nonuniform Traveling Field. In: *IEEE Transactions on Industry Applications* 24 (1988), Nr. 2

[NV03] Nieuwenhuis, J.H ; Vellekoop, M.J.: Improved Dielectrophoretic Particle Actuators for Microfluidics. In: *Proceedings of IEEE Sensors* 1 (2003), pp. 573–577

[OHCN09] Oh, J. ; Hart, R. ; Capurro, J. ; Noh, H.: Comprehensive analysis of particle motion uner non-uniform AC electric fields in a microchannel. In: *Lab on a Chip* 9 (2009), pp. 62–78

[PC71] Pohl, H. A. ; Crane, S.: Dielectrophoresis of cells. In: *Biophysical Journal* 11 (1971)

[PHWB92] Pethig, R. ; Huang, Y. ; Wang, X.B. ; Burt, J.P.H.: Positive and negative dielectrophoretic collection of colloidal particles using interdigitated castellated microelectrodes. In: *J. Phys. D: Appl. Phys* 24 (1992), pp. 881–888

[PJS+05] Pethig, R. ; Jakubek, L.M. ; Sanger, E. ; Corson, E.D. ; Smith, P.J.S.: Electrokinetic measurements of membrane capacitance and conductance for pancreatic β-cells. In: *IEEE Proc.-Nanobiotechnol.* 152 (2005), Nr. 6, pp. 189–193

[Poh51] Pohl, H. A.: The Motion and Precipitation of Suspensoids in Divergent Electric Fields. In: *Journal Of Applied Physics* 22 (1951), Nr. 7

[PT07] Pethig, R. ; Talary, M. S.: Dielectrophoretic detection of membrane morphology changes in Jurkat T-cells undergoing etoposide-induced apoptosis. In: *IET Nanobiotechnol.* 1 (2007), Nr. 1, pp. 2–9

[PTS03] Pethig, R. ; Talary, M. S. ; S., Lee R.: Enhancing Traveling-Wave Dielectrophoresis with Signal Superposition. In: *IEEE Engineering in Medicine and Biology Magazine* (2003)

[RZB+03] Rodolfi, L. ; Zittelli, C. G. ; Barsanti, L. ; Rosati, G. ; Tredici, M. R.: Growth medium recycling in Nannochloropsis sp. mass cultivation. In: *Biomolecular Engineering* 20 (2003), pp. 243–248

[SS85] Sauer, F. A. ; Schlögl, R. W.: Torques exerted on cylinders and spheres by external electromagnetic fields. A contribution to the theory of field induced rotation. In: *Interactions between electromagnetic fields and cells* (1985), pp. 33–42

[ST91] Schwan, H. P. ; Takashima, S.: Dielelectirc Behavior of Biological Cells and Membranes. In: *Bull. Inst. Chem. Res, Kyoto Univ.* 69 (1991), Nr. 4

[UT06] Urbanski, J.P. ; Thorsena, T.: Fast ac electro-osmotic micropumps with nonplanar electrodes. In: *Applied Physics Letters* 89 (2006)

[WHBG94] Wang, X-B. ; Huang, Y. ; Becker, F. ; Gascoyne, P.: A unified theory of dielectrophoresis and traveling wave dielectrophoresis. In: *J. Phys. D: Appl. Phys.* 27 (1994), pp. 1571–1574

[WHH+94] Wang, X-B. ; Hughes, M. P. ; Huang, Y. ; Becker, F. ; Gascoyne, P.: Nonuniform spatial distributions of both the magnitude and phase of AC electric fields determine dielectrophoretic forces. In: *Biochimica et Biophysica Acta* 1243 (1994), pp. 185–194

[WHW+97] Wang, X.-B. ; Huang, Y. ; Wang, X. ; Becker, F.F. ; Gascoyne, P.: Dielectrophoretic Manipulation of Cells with Spiral Electrodes. In: *Biophysical Journal* 72 (1997), pp. 1887–1899

[Wu08] Wu, J.: Interactions of electrocal fields with fluids: laboratory-on-a-chip applications. In: *IET Nanobiotechnol.* 2 (2008), Nr. 1, pp. 14–27

[WWG97] Wang, X. ; Wang, X-B. ; Gascoyne, P.: General expressions for dielectrophoretic force and electrorotational torque derived using the Maxwell stress tensor method. In: *Journal of Electrostatics* (1997), pp. 277–295

[WWK07] Wanichapichart, P. ; Wongluksanapan, T. ; Khooburat, L.: Electrorotation: Diagnostic Tool for Abnormality of Marine Phytoplankton Cells. In: *Proceedings of the 2nd IEEE International Conference on Nano/Micro Engineered and Molecular Systems* (2007)

[YHW+99] Yang, J. ; Huang, Y. ; Wang, X. ; Wang, X.-B. ; Becker, F.F. ; Gascoyne, P.: Dielelectric Properties of Human Leukocyte Subpopulations Determined by Electrorotation as a Cell Separation Criterion. In: *Biophysical Journal* 76 (1999), pp. 3307–3314